國立臺灣大學工學院材料科學與工程學系暨研究所

碩士論文

Department of Materials Science and Engineering

College of Engineering

National Taiwan University

Master Thesis

利用 3d 過渡金屬提升異質結構之自旋軌道矩轉換效率

Enhancing Spin-Orbit Torque Efficiency through 3d Transition Metal Modulation in Heavy Metal/CoFeB/MgO/Ta Heterostructure

陳冠豪

Kuan-Hao Chen

指導教授: 白奇峰 博士

Advisor: Chi-Feng Pai, Ph.D.

中華民國 112 年 6 月

June, 2023

doi:10.6342/NTU202301664

國立臺灣大學碩士學位論文
口試委員會審定書

論文中文題目： 利用 3d 過渡金屬提升異質結構之自旋軌道矩轉換效率

論文英文題目： Enhancing Spin-Orbit Torque Efficiency through 3d Transition Metal Modulation in Heavy Metal/CoFeB/MgO/Ta Heterostructure.

本論文係**陳冠豪**君**(R10527051)**在國立臺灣大學材料科學與工程學系、所完成之碩士學位論文，於民國 112 年 6 月 26 日承下列考試委員審查通過及口試及格，特此證明

口試委員： 白奇峰 白奇峰
（指導教授）

宋明遠 宋明遠

黃榮俊 黃榮俊

____

____

系主任、所長 蔡豐羽 蔡豐羽 （簽名）

doi:10.6342/NTU202301664

Acknowledgements

從大四開始在實驗室當專題生一直到現在碩士班二年級，非常感謝白奇峰老師的詳細指導。老師在研究方面時常給我點了盞明燈，也花時間和我討論題目的可行性。除此之外，在我對於出國攻讀博士班與否有所疑慮時，老師也會不吝嗇地分享經驗並給予幫助。特別感謝天玥學長和唯邦學長在我還是專題生的時候手把手的帶我步入磁性的學術殿堂，在我對這領域還懵懵懂懂的時候給予我學習的方向以及關心我的進度，讓我在正式進入碩班時期能夠自立自強。感謝 Neil 和佑展學長傳授實驗室儀器的程式撰寫技巧，使得日後量測上能自行解決程式問題。也非常感謝彥廷學長、宸瑜學長以及宇豪學長在我對於量測原理和期刊文獻有不理解之處，也能細心的和我解釋並提供有建設性的建議。

由衷感謝子翔、成瑋、庭瑀、郁芳、建平等學長姊給予我量測方面的教學以及量測技巧的傳授，讓我學習到了很多小撇步。也謝謝永誠、兆中、佳晉願意花時間和我討論文獻、實驗結果以及碩班課業，讓我常常醍醐灌頂，感受到他們強大之處，收穫良多。此外，謝謝瑋德、詩哲、東岳、俊逸、芷琳和我當量測夥伴一起聊天，當我的快樂泉源。

感謝社團的朋友時常帶給我歡樂和幸福，和你們相處時積累的壓力都煙消雲

doi:10.6342/NTU202301664

散，碩班生涯裡充斥著你們的笑聲和美好的記憶。最後真誠感謝爸媽和姊姊的支持，你們的關心和鼓勵時時刻刻激勵著我，造就了我碩班兩年的精華，也成為了我的支柱。

摘要

隨著近年來摩爾定律已經發展到盡頭，儘管有修正的摩爾定律版本，但是仍須一些特殊的技術來支持。這時，次世代記憶體越來越受到重視以及獲得許多認可。其中，最有名的磁阻式隨機存取記憶體具有非揮發性、能量消耗較低的特性因此備受矚目，其中以自旋軌道矩式磁阻式隨機存取記憶體 (SOT-MRAM) 的表現最為優異，包含了快速寫入、高耐久度以及低寫入電流的特性使它具備良好的競爭力。

利用合金供給自旋電流可以有效提升類阻尼自旋軌道矩效率。然而所使用的金屬成本都不低，這對於未來在量產磁阻式隨機存取記憶體會是一大難題。因此在本篇論文，會使用相對便宜以及自然界含量高的鎢、鈷、鈦金屬來製作合金以及多層膜，其中包含了鎢鈷合金、鎢鈷多層膜、鎢鈦多層膜。我們利用這些合金或多層膜當作自旋電流供給方並進行量測，發現在類阻尼自旋軌道矩效率擁有卓越的表現；而多層膜也擁有很小的翻轉電流，進而在較低的電壓下也能進行翻轉，避免造成元件的擊穿現象。本篇期望能帶給自旋軌道矩式磁阻式隨機存取記憶體一點啟發。

關鍵字：自旋電子學、自旋軌道矩式記憶體、自旋軌道矩、合金、多層膜、類阻

doi:10.6342/NTU202301664

尼自旋軌道矩效率

Abstract

As we approach the end of the Moore's Law, the significance of next generation memories has become increasingly prominent in recent years. Among these, Magnetoresistive Random Access Memory (MRAM) has emerged as a promising nonvolatile memory, with spin-orbit torque MRAM (SOT-MRAM) being competitive. The SOT-MRAM possesses several desirable properties, such as high writing speed, high endurance, and low writing current. Furthermore, considering the environmental and economic concerns, a SOT-MRAM should exhibit high damping-like efficiency (ξ_{DL}), excellent thermal stability, and low power consumption.

Alloys are regarded as a promising substitution of heavy metal (HM) layer for future advancements, as they provide enhancements in both spin Hall angle (θ_{SH}) and ξ_{DL} while maintaining a moderate resistivity. Numerous experimental studies conducted by different research groups have confirmed the enhancements in θ_{SH} and ξ_{DL} achieved through

doi:10.6342/NTU202301664

the use of different alloys. However, the composition of these alloys can be costly, posing challenges for mass production.

In this thesis, we explore the utilization of not only alloys but also multilayers as the HM layer. WCo alloy, WCo multilayer, WTi multilayer demonstrate enhancement in ξ_{DL}. Moreover, both multilayers possess extremely low switching currents, which effectively contributes to reducing the applied voltages across the devices.

Keywords: Spintronics, SOT-MRAM, Spin Hal Effect, Spin-Orbit Torque, Alloy, Multilayer, Damping-Like Spin-Orbit Torque Efficiency

Contents

doi:10.6342/NTU202301664

doi:10.6342/NTU202301664

doi:10.6342/NTU202301664

doi:10.6342/NTU202301664

List of Figures

List of Tables

doi:10.6342/NTU202301664

Denotation

AHE	Anomalous Hall Effect
PMA	Perpendicular Magnetic Anisotropy
SHE	Spin Hall Effect
SOC	Spin-Orbit Coupling
LM	Light Metals
HM	Heavy Metals
FM	Ferromagnetic Metals
STT	Spin-Transfer Torque
SOT	Spin-Orbit Torque
dc	Direct Current
MRAM	Magnetoresistive Random Access Memory
H_c	Coercivity Field

doi:10.6342/NTU202301664

DL	Damping-like
BCC	Body-Centered Cubic

Chapter 1 Introduction

1.1 Hall Effect

The term ”Hall effect” was originally coined to describe the generation of voltage perpendicular to an electric current in the presence of a magnetic field. However, over the past few decades, the term has been widely used to encompass any phenomenon where a voltage signal emerges in the transverse direction, regardless of the application of a magnetic field. Consequently, there have been numerous variations of the Hall effect, such as quantum Hall effect[1], quantum anomalous Hall effect[2], and quantum spin Hall effect[3], which is shown in Fig.1.1(d-f). It is important to note that these novel effects are not covered in this thesis.

1.1.1 Ordinary Hall Effect

The Hall effect describes the phenomenon where a magnetic field applied perpendicular to an electric current flowing through a conductor in the longitudinal direction creates a measurable voltage difference across the conductor. Discovered by Edwin Hall in 1879[5], it is characterized by the generation of a voltage in the transverse direction.

doi:10.6342/NTU202301664

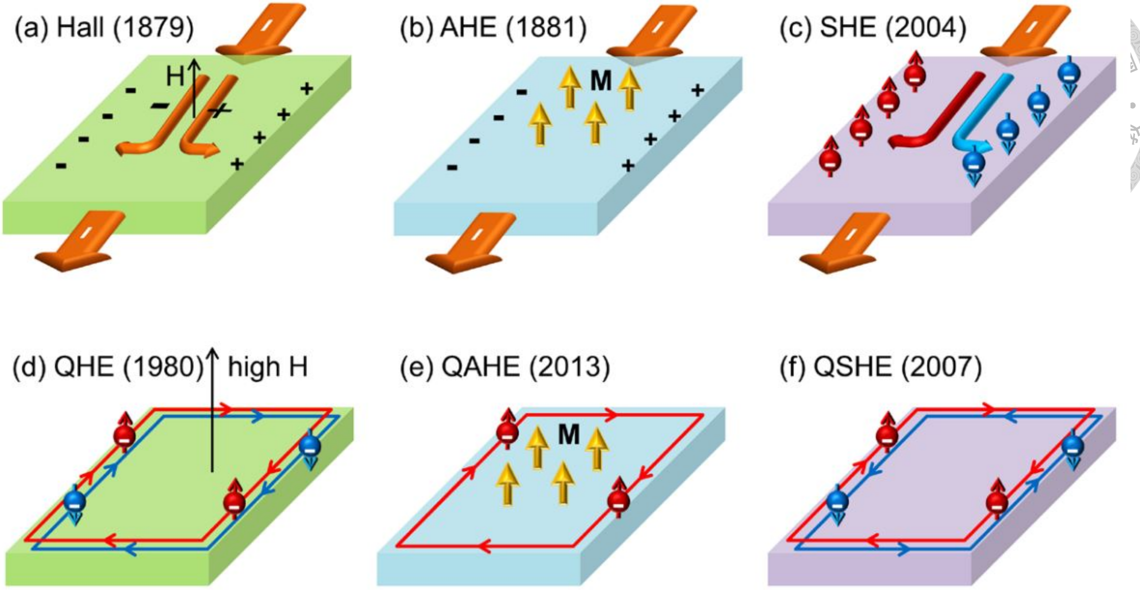

Figure 1.1: Schematic plots of varying Hall effects[4].

When an electric current flows through a conductor, such as a metal or a semiconductor, the moving charges experience a Lorentz force due to the magnetic field, which is expressed as equ.1.1:

$$\mathbf{F} = \mathrm{q}\left(\mathbf{E} + \mathbf{v} \times \mathbf{B}\right), \tag{1.1}$$

where **F** is the Lorentz force, **v** is the velocity of charge, and **E** and **B** are the electric field and the magnetic field, respectively. In the presence of a perpendicular magnetic field, the charged particles are deflected to one side of the conductor, resulting in an accumulation of electron on that side and an accumulation of hole on the opposite side. This charge separation creates an electric field that opposes the further accumulation of electron and hole. This equilibrium leads to the development of a voltage across the conductor, known as the Hall voltage.

The Hall coefficient, denoted as R_{H}, is a parameter that characterizes the Hall effect in a material.

$$R_{\mathrm{H}} = \frac{E_y}{j_c B_z} = \frac{1}{ne}, \tag{1.2}$$

It provides information about the charge carriers present in the material. The sign of the R_{H} determines the type of charge carriers: negative for electrons and positive for holes. It is used to study the electrical and magnetic properties of materials, including their carrier concentration, mobility, and conductivity.

The Hall effect has practical applications in various fields. Hall effect sensors, for example, are used to measure magnetic fields and detect current in sensors. Additionally, the Hall effect is utilized in solid-state physics to study the electrical properties of materials. It has played a crucial role in understanding charge carriers and has paved the way for the exploration of related phenomena, such as the quantum Hall effect and other advanced variations discussed in the beginning.

1.1.2 Anomalous Hall Effect

The anomalous Hall effect (AHE) is a phenomenon observed in condensed matter physics where a transverse voltage, known as the Hall voltage, is generated in the absence of an external magnetic field, especially in ferromagnetic materials. The AHE is also discovered by Edwin Hall while he was conducting the Hall measurement for ferromagnetic materials. Unlike the ordinary Hall effect, which is primarily driven by Lorentz force acting on charge carriers, the AHE involves additional contributions related to spin-orbit interaction (SOI) and magnetization. In ferromagnetic materials, magnetization plays a

doi:10.6342/NTU202301664

crucial role as an effective magnetic field that interacts with the charge carriers. The amount of spin-up currents and spin-down currents are different, and they possess opposite transverse velocities, resulting in unequal charge accumulations on opposite sides of the material. As a consequence, a voltage develops across the ferromagnetic material[6]. In addition, if the magnetic field is applied, both the ordinary Hall effect and the anomalous Hall effect coexist, following equ1.3.[7]:

$$R_{\mathrm{xy}} = R_{\mathrm{O}} H_z + R_{\mathrm{A}} M_z, \tag{1.3}$$

where R_{A} is much larger than R_{O} in ferromagnetic materials, and the square hysteresis loop can be obtained.

As depicted in Fig.1.2, there are three kinds of mechanisms to affect the AHE, including intrinsic deflection, side jump, and skew scattering[8].

Intrinsic mechanism: It was first proposed by Karplus and Luttinger in 1954[6]. It states that when a solid is subjected to an external electric field direction, electrons acquire an anomalous group velocity perpendicular to the electrical field, which gives rise to a nonzero Hall voltage value in ferromagnetic materials. This effect is closely associated with the Berry curvature and Berry phase[9], which are connected to the band structure of the materials. Importantly, the intrinsic mechanism is not influenced by defects but rather relies on the inherent properties of the material. Hence, it is referred to as intrinsic[10–13].

Side jump: The concept of the side jump was first introduced by Berger in 1970[14]. With the presence of defects or impurities in the crystal lattice, electrons with opposite spin orientations, namely spin-up and spin-down, experience deflections as they approach and depart from these impurities due to the opposite electric field they experience[7, 15].

Skew scattering: The concept of skew scattering was first introduced by Smit in 1955 and 1958[16, 17]. It describes the phenomenon where electrons with opposite spins exhibit asymmetric scattering behavior when encountering defects or impurities, influenced by the SOI. Both the side jump and skew scattering are considered extrinsic mechanisms since they interact with defects or impurities.

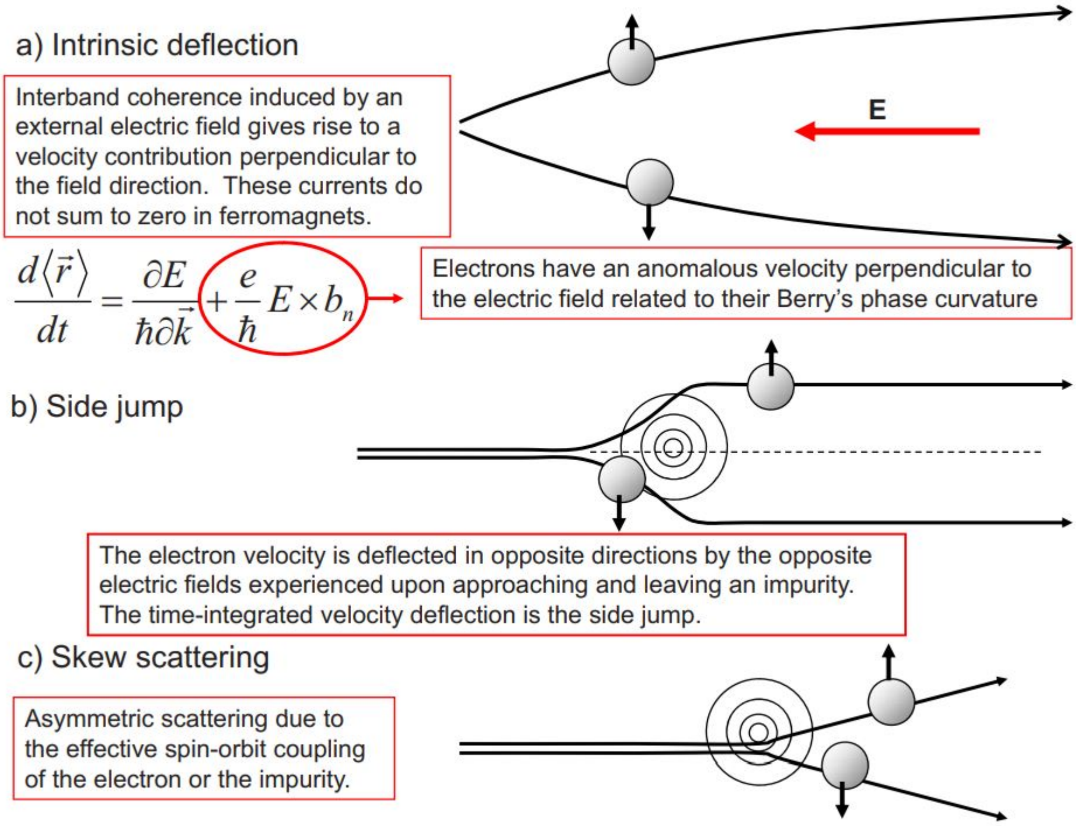

Interband coherence induced by an external electric field gives rise to a velocity contribution perpendicular to the field direction. These currents do not sum to zero in ferromagnets.

$$\frac{d\langle\vec{r}\rangle}{dt} = \frac{\partial E}{\hbar\partial\vec{k}} + \frac{e}{\hbar}E\times b_n$$

Electrons have an anomalous velocity perpendicular to the electric field related to their Berry's phase curvature

The electron velocity is deflected in opposite directions by the opposite electric fields experienced upon approaching and leaving an impurity. The time-integrated velocity deflection is the side jump.

Asymmetric scattering due to the effective spin-orbit coupling of the electron or the impurity.

Figure 1.2: Mechanism of anomalous Hall effect[8].

1.1.3 Spin Hall Effect

The spin Hall effect (SHE) is a phenomenon in condensed matter physics where an electric current induces a spin polarization perpendicular to the direction of the current

doi:10.6342/NTU202301664

flow. The mechanisms behind the SHE and the AHE are quite similar. Both involve deflections in opposite directions as electrons with different spins encounter impurities, including intrinsic mechanism, skew scattering, and side jump which is shown in Fig.1.3(a-c)[18]. However, the AHE usually occurs in ferromagnetic materials and arises from an imbalance in the number of electrons at the Fermi level, resulting in the generation of a Hall voltage. On the other hand, the SHE typically occurs in normal metals (NM) and is driven by the spin-orbit coupling (SOC) in which depicted Fig.1.3(d)[19]. It makes the amounts of deflected electrons on the opposite sides remain equal. As a result, the Hall voltage resulting from the SHE cannot be directly measured using conventional electrical methods, for the accumulation of deflected electrons is symmetric[20].

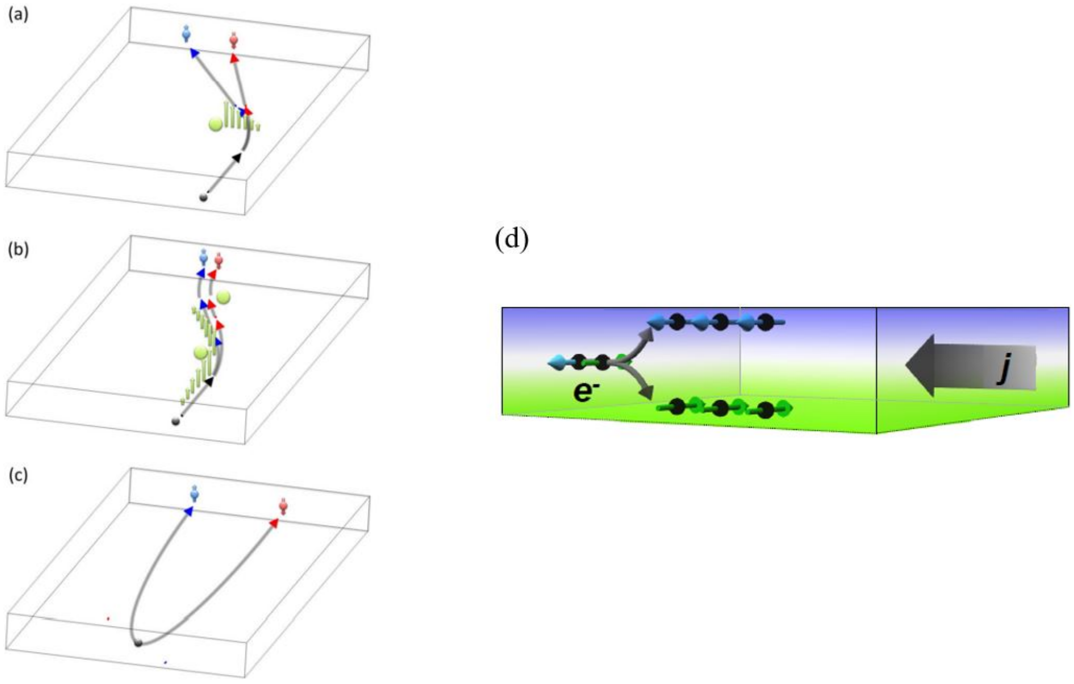

Figure 1.3: Schematic plots of different mechanisms contributing to the SHE and the AHE. (a) skew scattering. (b) side jump. (c) Intrinsic spin Hall effect. (d) Schematic plot of the deflected charge currents due to the SHE[18, 21].

Therefore, in order to analyze the SHE, a commonly employed method is to introduce breaking the inversion symmetry. With a ferromagnetic layer deposited in proximity to the heavy metals (HM) layer, the spin accumulated at the surface transfers the angular momentum to the magnetic moments within the ferromagnetic layer. This transfer further brings about the spin-orbit torque (SOT), resulting in the magnetization switching in the ferromagnetic layer, specifically the ferromagnetic layer with perpendicular magnetic anisotropy (PMA) property. The initial confirmation of the SHE was achieved through the analysis using the magneto-optical Kerr effect (MOKE) technique, as shown in Fig.1.4. The MOKE images reveal the spins with opposite polarization accumulated on opposite sides, providing evidence for the existence of SHE[22].

In addition, the strength of SHE is influenced by the strength of SOC, heavy metals typically exhibit significant SHE due to their strong SOC, including Pt, W, and Ta, whereas 3d transition metals typically demonstrate a weaker SHE owing to their low atomic numbers, such as Ti, V, and Mn. The equation of the SHE can be expressed as:

$$\boldsymbol{J_s} = \frac{\hbar}{2e}\theta_{\mathrm{SH}}(\hat{\boldsymbol{\sigma}} \times \boldsymbol{J_e}), \tag{1.4}$$

where $\hat{\boldsymbol{\sigma}}$ represents the spin polarization of the charge current, θ_{SH} corresponds to the spin Hall angle, which serves as a benchmark for assessing the efficiency of charge-to-spin conversion. Additionally, $\boldsymbol{J_s}$ and $\boldsymbol{J_e}$ denote the spin current density and charge current density, respectively[19, 23–25].

doi:10.6342/NTU202301664

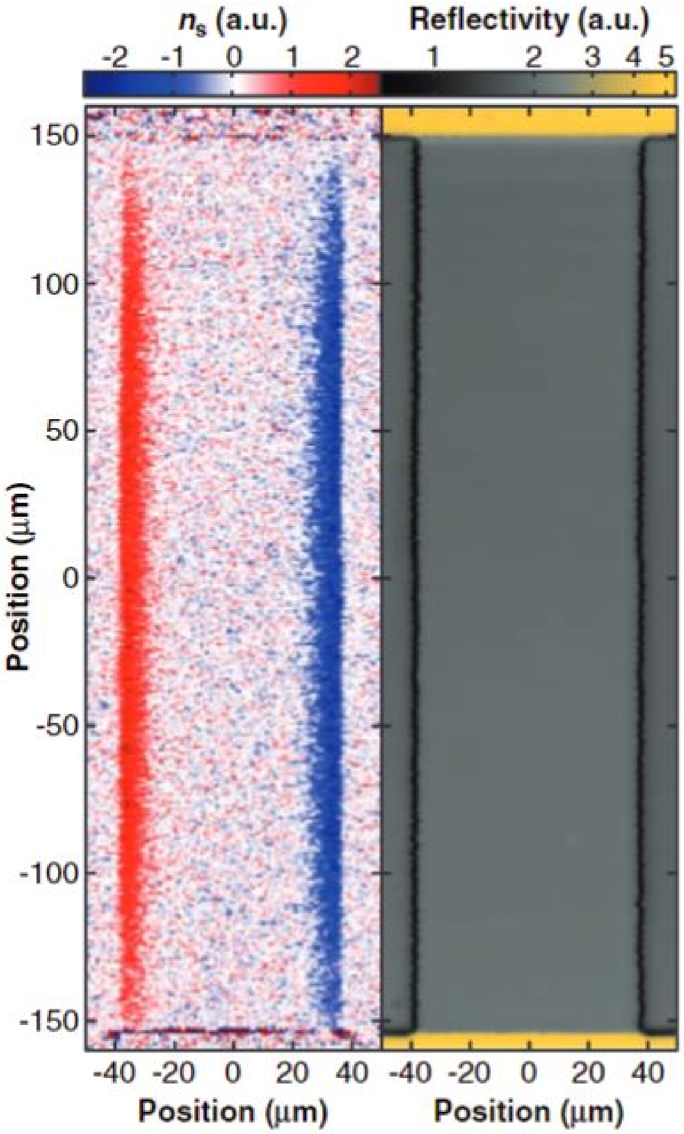

Figure 1.4: The MOKE images of GaAs sample, indicating the presence of accumulated spins on opposite sides[22].

1.2 Spin Hall Conductivity

To determine the strength of the SHE, not only the θ_{SH} can evaluate the efficiency of charge-to-spin conversion, spin Hall conductivity, denoted as σ_{xy} or σ_{SH} can also be an indicator of the SHE. As mentioned in the previous section, the SHE comprises both an intrinsic and an extrinsic component. The intrinsic spin Hall conductivity can be mathematically expressed as[26]:

$$\sigma_{\text{xy}}^{\text{intrinsic}} = \frac{e}{4a}\frac{\langle l \cdot s\rangle_{FS}}{\hbar^2}, \tag{1.5}$$

where a is the lattice constant, and $\langle l \cdot s\rangle_{FS}$ represents spin-orbit interaction at the Fermi level which is closely linked to the band structure of the perfect crystal. The extrinsic mechanisms of the SHE involve both skew scattering and side jump, with the spin Hall conductivity $\sigma_{\text{xy}}^{\text{side jump}} \propto \sigma_{\text{xx}}^2$[14] and $\sigma_{\text{xy}}^{\text{skew}} \propto \sigma_{\text{xx}}$[16], respectively. The overall spin Hall conductivity can then be the form of equ.1.6[20, 27].

$$\sigma_{\text{xy}}^{\text{H}} = \sigma_{\text{xy}}^{\text{int}} + \sigma_{\text{xy}}^{\text{side jump}} + \sigma_{\text{xy}}^{\text{skew}}, \tag{1.6}$$

In addition, when the SHE measurement is conducted under low temperature, the effect of skew scattering can be ignored, remaining intrinsic and side jump mechanisms. In this thesis, the measurement under variation temperatures are not conducted, so the σ_{SH} in the text includes both intrinsic and extrinsic components. Furthermore, a summary of experimental measured σ_{SH} is shown in Fig.1.5[28].

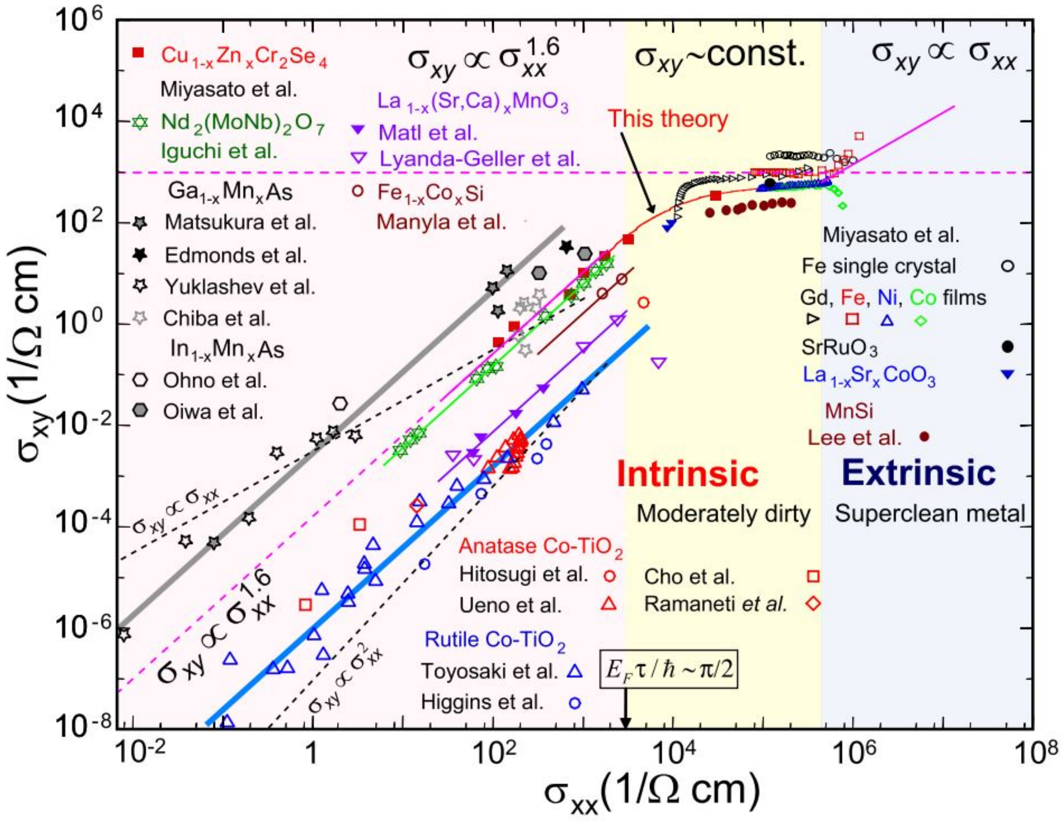

Figure 1.5: A summary of experimental results of σ_{SH} on various ferromagnetic materials[28].

1.3 Spin-Orbit Torque

Spin-orbit torque arises from the SHE and the Rashba Edelstein effect (REE). Both of these mechanisms contribute to the generation of spin accumulation at the interface, enabling the injection of spin current and spin momentum into the ferromagnetic (FM) layer in which depicted Fig.1.6(a-b)[29]. In contrast to spin-transfer torque (STT), which requires two FM layers, one fixed layer and one free layer, the spin in the current is polarized by the fixed layer and injected into the free layer and switches the magnetic moments in the free layer. The application of SOT in the field of MRAM solves the breakdown issue of magnetic tunneling junction (MTJ). This experiment was accomplished by Miron *et al.*[30] with the PMA sample structure Pt/Co/AlO$_x$. The SOT-MTJ is first done by Liu *et al.*[31] by measuring the Ta/CoFeB/MgO/CoFeB heterostructure, and it has a brilliant result, as shown in Fig.1.6(c-d).

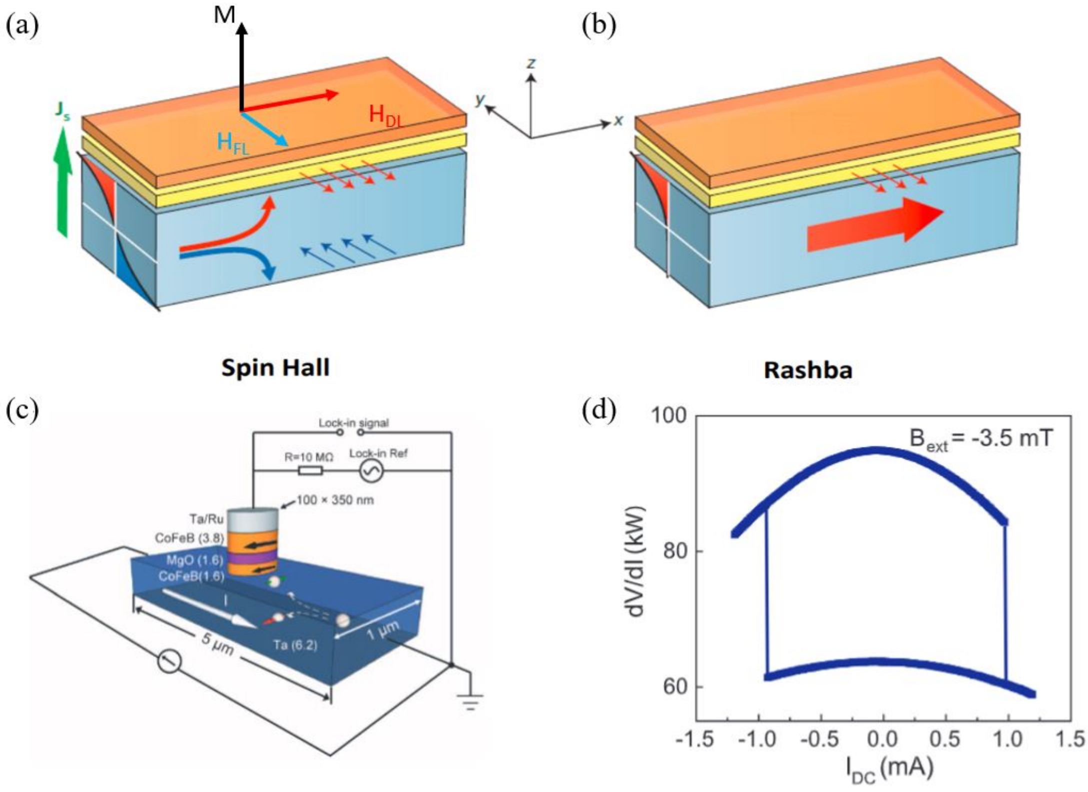

Figure 1.6: Shematic plots of (a) SHE and (b) REE[29]. (c) The sample structure of the first SOT-MTJ. (d) The tunneling magnetoresistance (TMR) of Ta/CoFeB/MgO/CoFeB heterostructure[31].

In addition, the perturbation resulting from the SOT can be described using the Landau-Lifshitz-Gilbert-Slonczewski (LLGS) equation, initially proposed by Lev Landau, Evgeny Lifshitz, and T.L. Gilbert. This equation was later revised by Slonczewski, who introduced the concept of the STT. The LLGS equation constructs the magnetization trajectory model describing its overall dynamics, which is shown in equ.1.7[32–34].

$$\frac{\partial \mathbf{m}}{\partial t} = -\gamma \mathbf{m} \times \mathbf{H}_{\text{eff}} + \alpha \mathbf{m} \times \frac{\partial \mathbf{m}}{\partial t} + \beta\gamma \left[c_{\text{DL}} \mathbf{m} \times (\mathbf{m} \times \boldsymbol{\sigma}) + c_{\text{FL}} \mathbf{m} \times \boldsymbol{\sigma} \right], \tag{1.7}$$

where γ is the gyromagnetic ratio, α is the Gilbert damping constant, $\beta = \frac{J_e \hbar}{M_s e t_{FM}}$, M_s represents the saturation magnetization of the FM layer, and $\mathbf{H}_{\text{eff}}$ is the overall effective field, including the external magnetic field, exchange interaction field, and anisotropy field, etc. The first term in the equation describes the in situ precession behavior of the magnetization resulting due to the influence of the overall effective field. While the second term indicates the damping behavior, making the magnetization gradually align with the direction of $\mathbf{H}_{\text{eff}}$. The third and fourth terms illustrate the DL-SOT and field-like torque, arising from the generation of spin currents via the SOC. The DL-SOT competes with the damping term and is also known as the anti-damping torque, as depicted in Fig1.7.

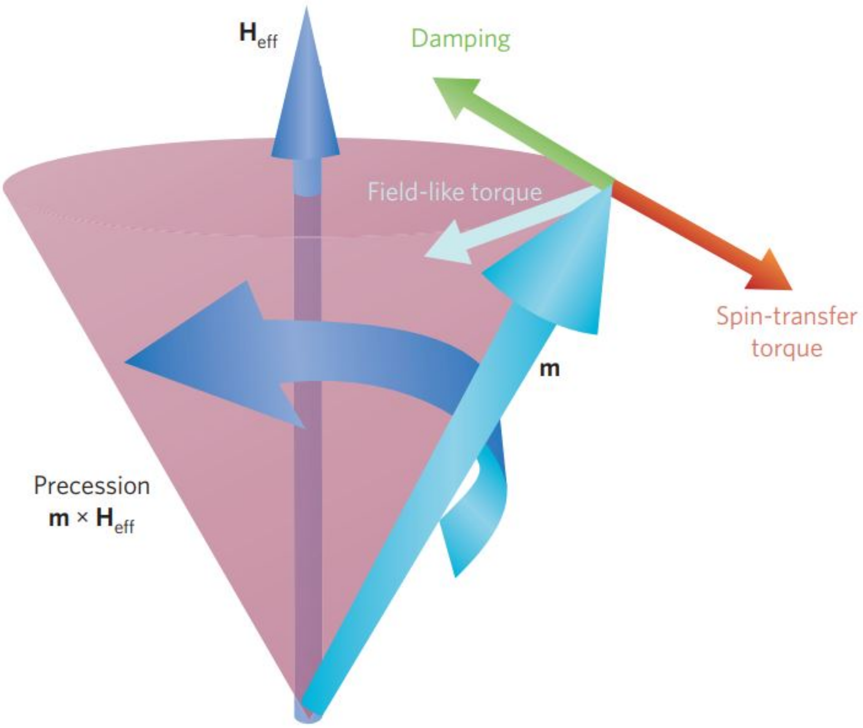

Figure 1.7: Schematics plot of the LLGS equation[33].

1.4 Motivation of This Work

Nowadays, reducing power consumption (P) is a significant concern in the SOT-MRAM. Power consumption can be affected by the resistivity and the current density of the heavy metal with the relationship illustrated in equ1.8.

$$P \propto \rho_{\mathrm{HM}} \cdot J_{\mathrm{HM}}^2, \tag{1.8}$$

In order to reduce power consumption, it is prior to find a substitution to lower both ρ_{HM} and J_{HM}. However, damping-like efficiency (ξ_{DL}) is directly proportional to the ρ_{HM} and inversely related to J_{HM}. Therefore, there is a challenging trade-off between ρ_{HM} and J_{HM}. On one hand, higher values of ρ_{HM} result in high ξ_{DL} but but they also lead to higher power consumption.

Furthermore, based on the Moore's law, the sizes of electronic components nowadays tend to be minimized, making a possibility to display more components or devices on a printed circuit board. However, the smaller size of electronic components, the harder the yield we obtain. Therefore, a thick HM layer with a strong ξ_{DL} and a small switching current makes our MTJ high and easily etched, which effectively maintains the yield[35].

Alloys are considered as an up-and-comer because they offer improvements in both θ_{SH} and ξ_{DL} while maintaining a moderate resistivity. Numerous studies claim that the use of varying alloys have enhancement on θ_{SH} and ξ_{DL}. However, selecting the appropriate dopant elements remains a challenge in the field. Extensive research is being conducted

doi:10.6342/NTU202301664

on Pt-based alloys, including PtCu alloy[36, 37], PtAu alloy[38], PtAl and PtHf alloy[39], PtGd alloy[40], etc. In contrast, for W-based alloys, such as WHf alloy[41], WTa and WV alloy[42], are relatively going begging. In addition, alloys like AuTa[43], CuTa alloy[44], and AuCu alloy[45], etc. are examined by different groups. Moreover, in our lab, WV alloy, PtV alloy, and PtCr alloy are analyzed by Yu Fang, Chiu.

In this thesis, considering the desirable properties of tungsten, such as high θ_{SH}, excellent thermal annealing stability, and cost-effectiveness, we have chosen the WCo alloy as a HM layer. In addition, due to the formation of multilayers can be easily controlled, WCo multilayer is a substitution of HM layer. Moreover, we have also adopted WTi multilayer as a spin source. Both multilayers exhibit enhanced ξ_{DL} compared to pure tungsten control samples, and they demonstrate extremely low switching currents, contributing to the extremely low applied voltage which can avoid breakdown issues. Besides, thick HM layers with strong ξ_{DL} and small switching currents have the potential to maintain the yield during the production process of the devices, especially in the etching process.

Chapter 2 Sample Preparation

2.1 Thin Film Fabrication Techniques

2.1.1 Magnetron Sputtering

Sputtering is a physical vapor deposition (PVD) technique used to deposit thin films of various materials onto a substrate. The principle of sputtering involves harnessing a plasma generated by applying an electric potential difference, which is then directed towards bombarding the surface of a target material. As a result of this energetic collision, atoms from the target are expelled into the surrounding chamber space and subsequently adhere to the surface of the substrate, forming a deposited film. An incorporation of a magnetron technique into the sputtering process serves to significantly enhance the efficiency of sputtering. The magnetron sputtering machine in our lab consists of a vacuum chamber operating at an ultra-high vacuum level of approximately 10^{-8}Torr. It is equipped with multiple guns, each housing different targets, and an argon pipe serves as the plasma source for generating the plasma. This setup is depicted in Fig.2.1(a). The operational schematic of the magnetron is illustrated in Fig.2.1(b). The arrangement includes multiple magnets positioned beneath the targets. These magnets generate a magnetic field that effectively prolongs the lifetime of electrons within the plasma. This prolonged lifetime facilitates the motion of secondary electrons towards the vicinity of the target, thereby enhancing the efficiency of the sputtering process. Fig.2.1(c) shows the mechanism by which argon ions bombard the surface of the target, resulting in the emission of target atoms. In conclusion, magnetron sputtering is widely employed in industries such as electronics, and optics, offering the distinct advantage of facilitating mass production capabilities.

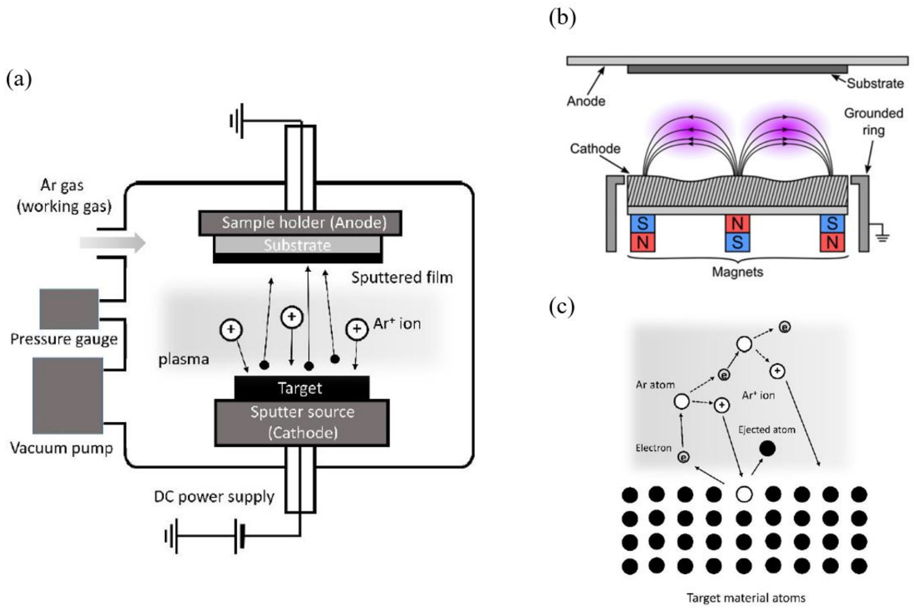

Figure 2.1: Schematics of sputtering deposition[46–48]. (a) A simplified sputtering system with a vacuum chamber, a target material, and a plasma source. (b) A schematic diagram of applying magnetron in a sputtering system. (c) The process of how a plasma ion bombard target material and the way target atoms are generated.

Target Element	W	Co	CoFeB	MgO	Ta	Ti (100W)
Growth Rate (nm/s)	0.03178	0.02647	0.01878	0.00333	0.03338	0.05056

Table 2.1: Summary of the sputter rates.

Atomic Ratio	W Power (W)	Co Power (W)	Alloy Growth Rate (nm/s)
$W_{0.7}Co_{0.3}$	50	10	0.05914
$W_{0.6}Co_{0.4}$	30	10	0.04562
$W_{0.5}Co_{0.5}$	30	20	0.04644
$W_{0.4}Co_{0.6}$	20	20	0.03830
$W_{0.32}Co_{0.68}$	30	50	0.06873
$W_{0.24}Co_{0.76}$	20	50	0.06365

Table 2.2: The sputter rates of WCo alloy.

The growth rates employed for depositing the samples in this study are presented in Table.2.1 and Table.2.2. These growth rates were calibrated using either the alpha step or the atomic force microscope (AFM). It is important to note that the values of the growth rates in the tables perform at 30 Watts unless otherwise specified.

2.1.2 Alloy Recipe

The formation of WCo alloys in this thesis is achieved through a co-sputtering technique, wherein two targets are simultaneously bombarded. This technique enables the precise control of the composition within the WCo alloy. The concentration of cobalt (X_{Co}) is calculated by the following equ.2.1:

$$X_{\mathrm{Co}} = \frac{r^{\mathrm{Co}}_{\mathrm{molar}}}{r^{\mathrm{W}}_{\mathrm{molar}} + r^{\mathrm{Co}}_{\mathrm{molar}}}, \tag{2.1}$$

where $r_{\text{molar}}^{\text{W}}$ and $r_{\text{molar}}^{\text{Co}}$ represent the molar growth rates of tungsten and cobalt, respectively.

In addition, it is necessary to calibrate the growth rates of tungsten and cobalt under different power conditions. This calibration process enables the determination of the molar growth rate for varying power settings. By utilizing equ.2.1, the atomic ratio values presented in Table.2.2 can be obtained. With the information of the power recipe and the specified concentration set, calibration samples are prepared by magnetron sputtering for a duration of 1000 seconds. These samples are subsequently calibrated using an alpha step measurement, and the obtained alloy growth data is shown in Table.2.2.

2.2 Photolithography

Photolithography is a crucial process used in microelectronic devices in semiconductor manufacturing to create patterns or designs on the surface of a substrate, usually a silicon wafer for instance. It involves a series of steps from the pattern on the photomask to the light-sensitive material, which is so-called a photoresist. The traditional processes of the photolithography process are composed of the following steps[49–51].

1. Substrate surface cleaning: To ensure the highest quality of patterns, it is essential to commence the photolithography process by thoroughly cleaning the silicon substrate using isopropanol (IPA). This preliminary step effectively eliminates dirt and organic contaminants that have the potential to hinder the pattern's quality and integrity.

2. Spin coating: Once the cleaning process is complete, the substrate is positioned on a rotary plate, ready for the application of a thin layer of positive photoresist. The recipe

doi:10.6342/NTU202301664

of spin coating is spun at 1000rpm for 10 seconds, ensuring a uniform distribution of the photoresist. This is followed by a rapid increase in speed to 4000rpm for 30 seconds, promoting the formation of a precise and smooth photoresist layer.

3. Soft bake: The purpose of the soft bake process is hardening the photoresist by a baking temperature of 100℃ for a duration of 7 minutes. It enhances the stability of the photoresist layer.

4. Exposing: By installing the photomask and utilizing UV light emitted by the mercury lamp, the UV light penetrates the photomask and transmits onto the photoresist. The desired patterns do exist.

5. Development: The positive photoresist is gently removed using a developer solution, tetramethylammonium hydroxide (TMAH). Through this process, the unwanted portions of the photoresist are dissolved, leaving behind Hall bar devices. These devices possess dimensions of $5\mu\text{m} \times 60\mu\text{m}$, which is shown in Fig.2.2.

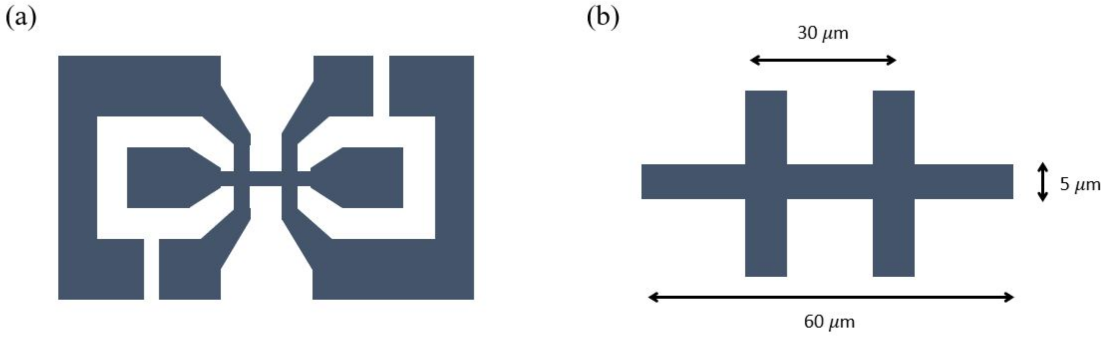

Figure 2.2: (a) Schematic plots and (b) the scale of Hall bar device.

Chapter 3 Measurement

3.1 Magnetic Property Characterization

3.1.1 Electrical Detection

To ensure the PMA property of each sample, Ordinary Hall measurement is conducted. As depicted in Fig.3.1(a), a dc current is applied along the longitudinal direction while scanning the out-of-plane magnetic field from negative to positive and then back to negative. This process allows us to obtain the anomalous Hall voltage in the transverse direction. When the sample exhibits a PMA property, the resulting anomalous Hall voltage exhibits a square loop pattern known as the hysteresis loop. The representative hysteresis loop is shown in Fig.3.1(b), and it represents the direction of the magnetic moments.

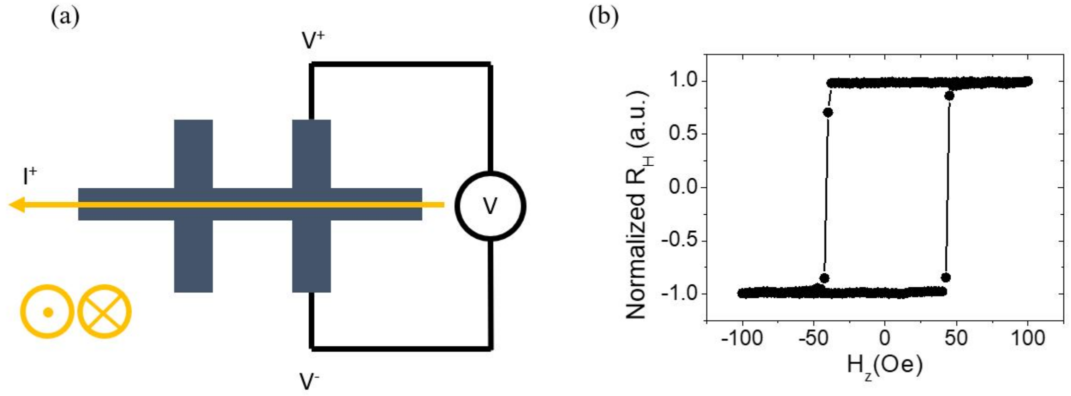

Figure 3.1: (a) Schematic plot of anomalous Hall measurement. (b) The representative hysteresis loop measured by the electrical method.

doi:10.6342/NTU202301664

To examine the stability of PMA, we normalize the anomalous Hall resistance ranging from +1 to -1. The stability is then quantified by the remanent magnetization ratio (M_R/M_S), where M_R can be obtained under $H_z = 0$ and M_S represents saturation magnetization[52–56].

3.1.2 Vibrating Sample Magnetometer

A vibrating sample magnetometer (VSM) is an advanced instrument used to measure the magnetic properties of materials. It operates on the principles of Faraday's Law, which states that when a magnetic field undergoes varying changes over time, it induces a magnetic flux. The magnetic flux will interact with the electric circuit, resulting in the generation of an electromotive force (emf). The relationship between the magnetic flux and emf can be described by the Maxwell–Faraday equation[57–59]:

$$\nabla \times \mathbf{E} = -\frac{\partial \mathbf{B}}{\partial t}, \tag{3.1}$$

where $\nabla\times$ is a curl operator, $\mathbf{E}(\mathbf{r}, t)$ and $\mathbf{B}(\mathbf{r}, t)$ is the electric field and magnetic field, respectively.

The process of conducting VSM measurement begins by affixing the sample onto a carbon stick. Subsequently, the carbon stick is positioned within a holder, which is hung between two electromagnets. During the VSM measurement, the magnetic field is set to a 1.5 Tesla (T), and the holder begins vibrating. The sample is exposed under a magnetic flux due to the effect of vibration. Consequently, the changing magnetic flux induces an emf, leading to the switching of magnetic moments. The VSM measurement can be employed to characterize the magnetic properties of various materials, including paramagnetic, ferromagnetic, etc.[60–64].

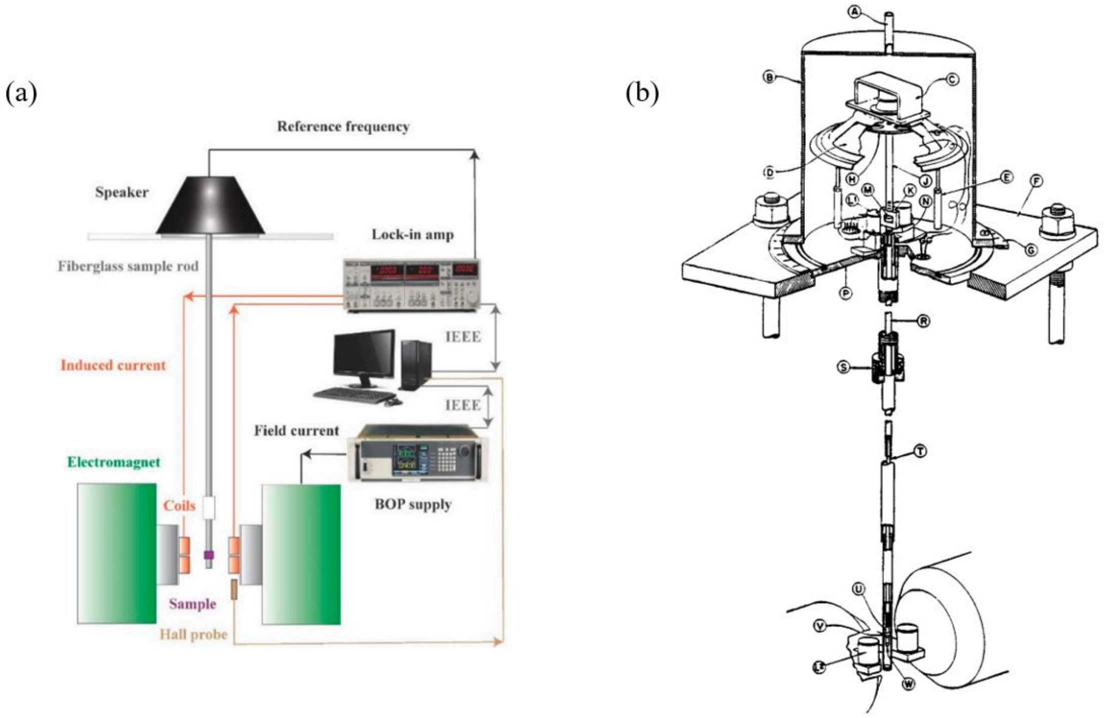

Figure 3.2: (a) Instrument setup of VSM[60]. (b) The anatomy chart of the VSM machine[61].

3.2 Spin-Orbit Torque Characterization

3.2.1 Hysteresis Loop-Shift Measurement

Hysteresis loop-shift measurement is a crucial technique used to analyze the SOT characterization of samples with PMA properties. It can characterize the DL efficiency (ξ_{DL}), the Dzyaloshinskii−Moriya interaction field (H_{DMI}), and the SOT effective field (H_{eff}^{z}). The mechanism of the hysteresis loop-shift measurement is based on the domain wall motion, as illustrated in Fig.3.3. Consider a scenario where three domains exist, with the magnetic moments inside two domains pointing upward and the remaining one pointing in the -z direction. Due to the opposite orientations of the domain walls, the magnetic moments located at the edges of the domains lie on the in-plane surface. When a charge current passes through the sample, the polarization (σ) of the spin current generated via SHE will affect the magnetic moments. Based on equ.1.7, the interaction between σ and magnetic moment results in the emergence of the $H_{\text{eff}}^{\text{z}}$, given by the relation $\mathbf{H}_{\text{eff}}^{\text{z}} = \boldsymbol{\sigma} \times \mathbf{m}$. Consequently, the magnetic moments at the edges of the domains experience an out-of-plane $H_{\text{eff}}^{\text{z}}$. As a result, all magnetic moments within the sample undergo changes in their orientations, with a velocity v_{DW}. However, since the directions of v_{DW} point in the same direction, there is no expansion of the domain wall, and the overall configuration remains unchanged. On the other hand, when an in-plane magnetic field is applied, the magnetic moments align in the same direction, resulting in the $H_{\text{eff}}^{\text{z}}$ being in the same direction. Affected by the $H_{\text{eff}}^{\text{z}}$, the magnetic moments start reorientation, causing the domain to move in the opposite direction, which means that v_{DW} are opposite and is shown in Fig.3.3(b). As a consequence, the domain wall expands, eventually resulting in the switching of the magnetic moment and the formation of a single domain within the sample[65, 66].

The setup of the hysteresis loop-shift measurement consists of a range of applied in-plane fields (H_{x}), a series of applied dc currents, the utilization of an out-of-plane magnetic field scanning the samples from negative to positive and back to negative, which is depicted in Fig.3.4(a). Based on the principle of the domain wall motion, when a constant H_{x} is applied, the hysteresis loops shift in opposite directions as opposite signs of dc currents are applied, which is illustrated in Fig.3.4(c). Additionally, if the sign of H_{x} is changed while keeping the dc current sign constant, the H_{eff}^{z} also changes its sign, as

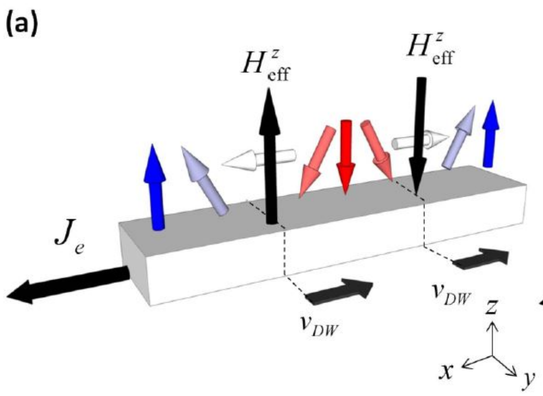

Figure 3.3: (a) Sechmatic of current-induced domain wall motion of a PMA sample without applying an external magnetic field. Domain walls move in the same direction, and it remains the same overall. (b) Schematic of current-induced domain wall motion of a PMA sample by applying an in-plane magnetic field. Domain walls then move in the opposite direction due to the effect of H_{eff}^{z}, resulting in the domain wall expansion[65].

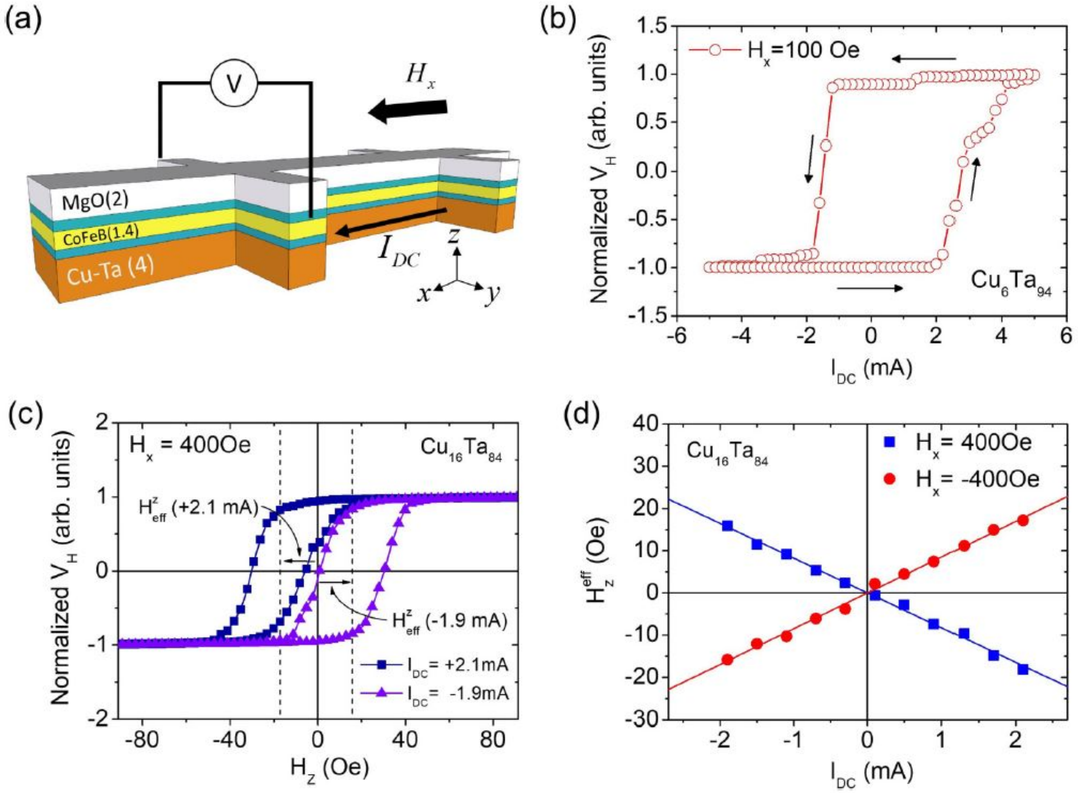

Figure 3.4: (a) Measurement setup of the hysteresis loop-shift measurement. (b) A representative current-induced SOT switching curve under H_{x} = 100Oe. The black arrows indicate the scanning direction of dc currents. (c) Representative hysteresis loop shift results under H_{x} = 400 Oe and I_{dc} = 2.1mA and -1.9mA, respectively. (d) H_{eff}^{z} as a function of I_{dc} under $H_{\mathrm{x}} = \pm$400Oe[44].

shown in Fig.3.4(d)[44, 66].

Furthermore, in the analysis of SOT characterization, a crucial parameter is the ξ_{DL}. The equation defining ξ_{DL} is presented in equ.3.2:

$$\xi_{\mathrm{DL}} = \left(\frac{2}{\pi}\right) \frac{2e}{\hbar} \mu_0 M_s t_{FM} w t_{HM} \left(1 + s\right) \left(\frac{H_{eff}^{z}}{I}\right), \tag{3.2}$$

$$s \equiv \frac{I_{FM}}{I_{HM}} = \frac{t_{FM}\rho_{HM}}{t_{HM}\rho_{FM}}, \tag{3.3}$$

where μ_0 is vacuum permeability, M_s and w are the situation magnetization and the width of HM layer, respectively, t_{FM} and t_{HM} are the thickness of FM layer and HM layer respectively. s is the current shunting parameter, as shown in equ.3.3. After conducting the hysteresis loop-shift measurement, $H_{\mathrm{eff}}^{\mathrm{z}}/I$ can be obtained. By substituting this ratio into equ.3.2, ξ_{DL} can be calculated[67, 68]. In addition, another expression of ξ_{DL} can be using current density (J) instead of dc current (I), which allows for more accurate comparison and analysis[66, 69]. In this thesis, the form of $H_{\mathrm{eff}}^{\mathrm{z}}/I$ is utilized.

3.2.2 Current-Induced Spin-Orbit Torque Switching Measurement

Current-induced SOT switching measurement is another important technique employed for analyzing the SOT characterization of samples exhibiting PMA properties. As discussed in the previous subsection, the application of H_{x} field is necessary to align the magnetic moments, counteract the influence of H_{DMI}, and disrupt the Néel type chiral domain wall. In the current-induced SOT switching measurement, the presence of H_{x} is needed to overcome these challenges. In the mechanism of current-induced SOT switching measurement, the role of the H_x is to compete with the depinning field of the domain wall (H_d). When $H_\text{x} < H_\text{d}$, the domain wall motion is significantly impeded by the disorder, which is the so-called creep law. Therefore, a higher magnitude of applied dc current is required, along with the increase of spin currents accompanied by the DL torque, to assist the magnetic moments overcome the hindering effects of H_d. Once H_x exceeds H_d, it can successfully overcome the depinning effect. Consequently, even if the applied current is relatively small, H_x can still motivate the domain wall motion, as illustrated in the previous subsection. As a result, the switching current will saturate to a constant value[70, 71].

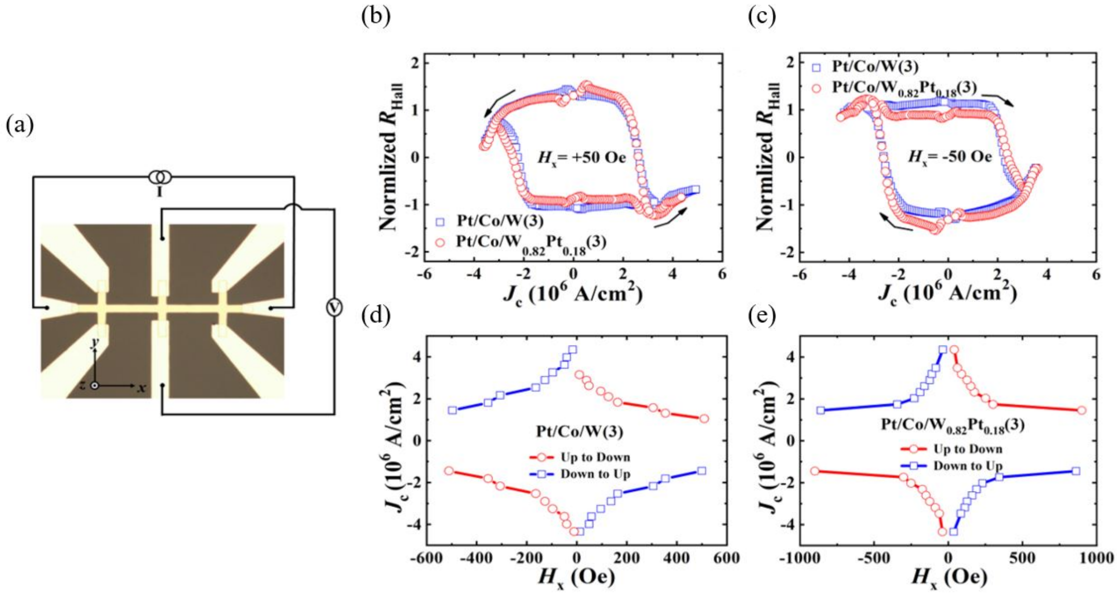

Figure 3.5: (a) The setup of the current-induced SOT switching measurement. (b)(c) The representative current switching loops. (d)(e) The relation between J_sw and H_x[72].

The measurement setup of the current-induced SOT switching is shown in Fig.3.5(a). This setup involves applying a H_x and a dc current along the longitudinal direction. The Hall voltage (V_H) is then measured in the transverse direction. Additionally, a small sensing current is employed to detect the magnetization switching. Fig.3.5(b-c) display the representative switching loops, illustrating the magnetization dynamics during the current switching process. Fig.3.5(d-e) show the relation between the switching current density J_{sw} and H_{x}[72, 73].

During the current-induced SOT switching measurement, significant thermal effects are generated due to the high applied value of dc current[74]. To eliminate the influence of these thermal effects, the measurement with a pulse width dependent analysis is conducted. This analysis enables the determination of the critical switching current (I_{c0}) without the influence of thermal effects and provides insights into the thermal stability factor (Δ). By changing the pulse width of the writing current (t_{pulse}), I_{c0} can be obtained by the following equation[37, 75]:

$$I_c = I_{c0}\left[1 - \frac{1}{\Delta}\ln\left(\frac{t_{pulse}}{\tau_0}\right)\right], \tag{3.4}$$

where $\tau_0 \approx$ 1ns, representing the intrinsic attempt time. $\Delta = \mathrm{U}/\mathrm{k_B T}$ signifies the thermal stability factor between the up state and down state in the PMA sample, with U representing the energy barrier, $\mathrm{k_B}$ is the Boltzmann constant, and T is the temperature. The values of I_{c0} and Δ can be obtained through a linear fitting of I_{c} and $\ln\left(\frac{t_{\mathrm{pulse}}}{\tau_0}\right)$. The equation of ξ_{DL} is a little different from the loop-shift measurement, which is shown in equ.3.5[76, 77]:

$$\xi_{\mathrm{DL}} = \left(\frac{2}{\pi}\right)\frac{2e}{\hbar}\mu_0 M_s t_{FM} w t_{HM}\left(1+s\right)\left(\frac{H_c}{I_c}\right), \tag{3.5}$$

3.3 Summary of Experiments

The sample structures in this thesis are depicted in Fig.3.6 & 3.7. The Heave metal (HM) includes pure tungsten, WCo alloy, WCo multilayer, and WTi multilayer. In addition, the t_{HM} in Fig.3.7 are 3.3, 5, 6.7, 8.1, and 10nm. The detailed recipe of WCo alloy, WCo multilayer, and WTi multilayer are shown in Table.2.2 to Table.3.2.

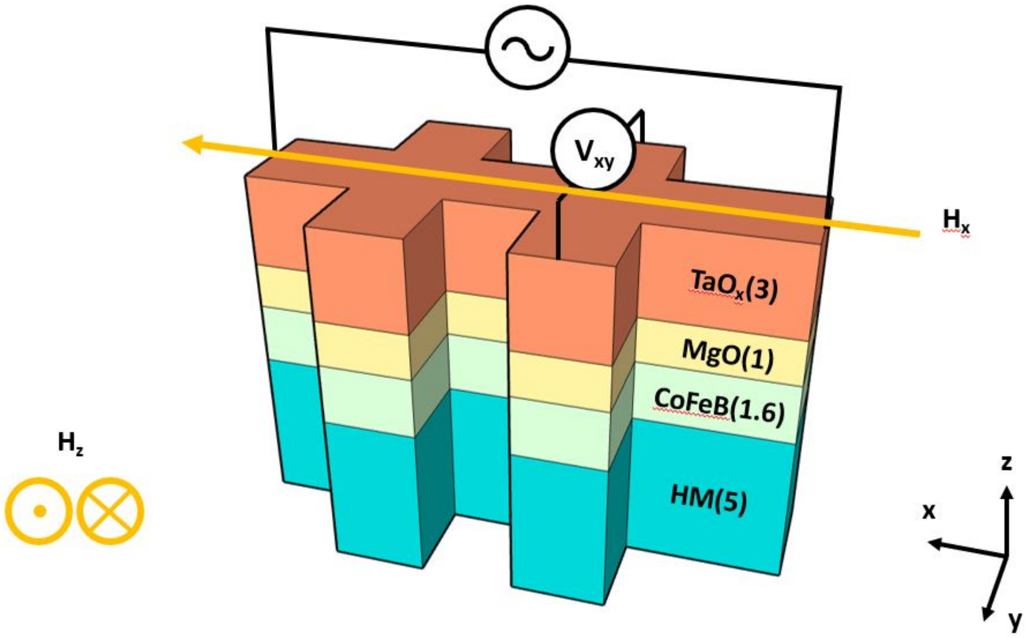

Figure 3.6: Schematic plot of the sample structure and the measurement setup.

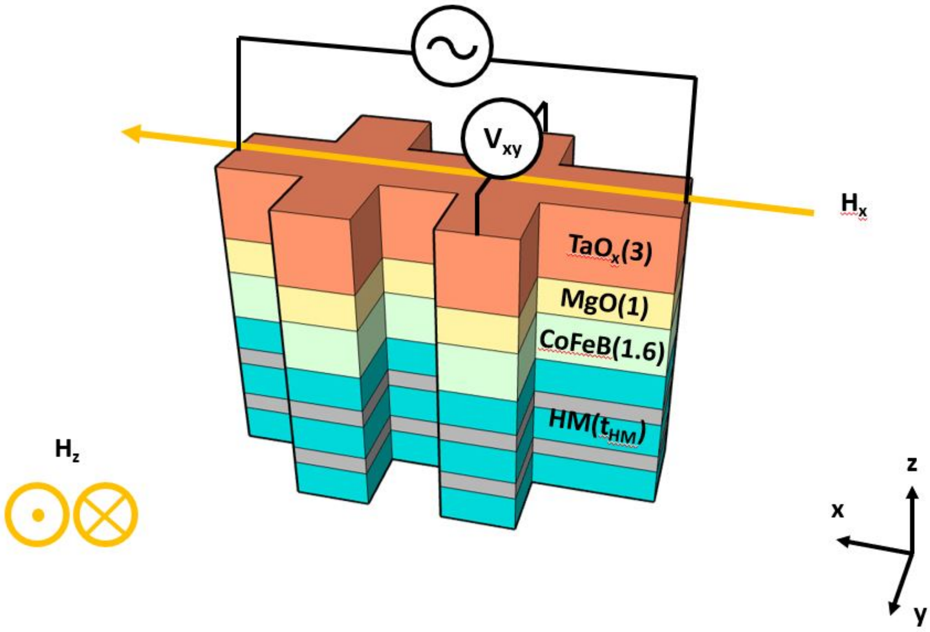

Figure 3.7: The sample structure with changing t_{HM} and the measurement setup.

Co thickness ratio	t_W (nm)	t_{Co} (nm)	$t_{W\ total}$ (nm)	$t_{Co\ total}$ (nm)
0	5	0	5	0
0.02	1.63	0.06	4.89	0.11
0.04	1.59	0.11	4.78	0.22
0.07	1.56	0.17	4.67	0.33
0.09	1.52	0.22	4.55	0.45
0.1	1.5	0.25	4.5	0.5
0.13	1.44	0.34	4.33	0.67
0.2	1.33	0.5	3.99	1
0.3	1.17	0.75	3.5	1.5
0.4	1	1	3	2
0.5	0.83	1.25	2.5	2.5
0.6	0.67	1.5	2	3

Table 3.1: The structure recipe of WCo multilayer.

Ti thickness ratio	t_W (nm)	t_{Ti} (nm)	$t_{W\ total}$ (nm)	$t_{Ti\ total}$ (nm)
0	5	0	5	0
0.024	1.63	0.06	4.88	0.12
0.047	1.59	0.12	4.76	0.24
0.071	1.55	0.18	4.64	0.36
0.1	1.5	0.25	4.5	0.5
0.2	1.33	0.5	4	1
0.3	1.17	0.75	3.5	1.5
0.4	1	1	3	2
0.5	0.83	1.25	2.5	2.5

Table 3.2: The structure recipe of WTi multilayer.

doi:10.6342/NTU202301664

Chapter 4 Spin-Orbit Torque Characterizations of WCo Alloy and Multilayer

The current-induced hysteresis loop-shift measurement is a widely used technique to measure PMA heterostructures. This technique involves the application of a series of direct currents and an in-plane magnetic field, which is parallel to the current's direction. A shifted hysteresis loop can be obtained by applying an out-of-plane magnetic field. This chapter focuses on the SOT characterization in the W/CoFeB control sample and explores the behavior of SOT when Co is doped into tungsten[65, 78].

4.1 W/CoFeB Control Samples

SOT characterization has traditionally focused on heavy metal(HM)/ferromagnetic metal(FM) heterostructures, with popular choices for the HM layer including Pt, W, etc, and for the FM layer, Pt/Co/Pt, CoFeB, CoFe, etc., are commonly used. While platinum's low resistivity can reduce the energy consumption in SOT-MRAM, the DL efficiencies of Pt/FM heterostructures have not met expectations. Therefore, tungsten then be a crucial spin source in HM/FM heterostructure due to its large DL efficiency. To analyze the SOT characterization, modulating the HM thickness is necessary. Based on the drift-diffusion model, the relation between the HM thickness dependent and the SOT efficiency is expressed by the spin diffusion model[32, 56, 67, 79, 80]:

$$|\xi_{\mathrm{DL}}(d_{\mathrm{HM}})| = \left|\xi_{\mathrm{DL}}^{0}\right| \left(1 - \operatorname{sech}\left(\frac{d_{\mathrm{HM}}}{\lambda_{\mathrm{sd}}}\right)\right), \tag{4.1}$$

where d_{HM} and λ_{sd} express the HM thickness and the spin-diffusion length, and ξ_{DL}^{0} is the bulk SOT efficiency, which is the saturated value under HM thickness dependence. Therefore, this section will discuss the SOT characterization of control samples: W(d_W)/CoFeB(1.6)/MgO(1)/Ta(3).

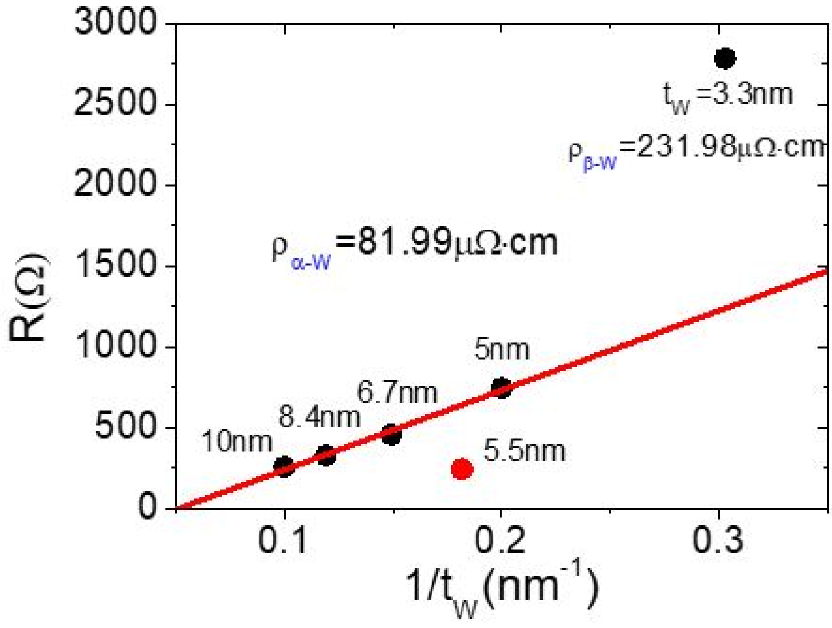

Figure 4.1: Resistivity fitting by the thickness dependence of tungsten. Captions inside the figure show the resistivity difference between α-W(BCC structure) and β-W(amorphous).

Based on Ohm's law, resistance is proportional to the thickness of materials, which is shown in equ.4.2.

$$R = \frac{\rho \cdot l}{w \cdot t}, \tag{4.2}$$

Where R, ρ are the resistance and resistivity, and l, w, and t are the length, width, and thickness of the specimen respectively. Fig.4.1 shows that resistance is linearly proportional to the reciprocal of tungsten's thickness. When the tungsten's thickness is thicker than 5nm, tungsten is a BCC structure, which is so-called α-W. In this region, resistance can be fitted well with the reciprocal of tungsten's thickness, and $\rho_{\alpha\text{-W}} = 81.99\mu\Omega \cdot \text{cm}$ is obtained from equ.4.2. However, when the tungsten's thickness is below 5nm, phase transition will occur, and it will turn into β-W with an amorphous phase. Meanwhile, the resistance and resistivity rise dramatically due to its non-crystalline structure, where $\rho_{\beta\text{-W}} = 231.98\mu\Omega \cdot \text{cm}$ as $t_W = 3.3\text{nm}$ [56, 76, 81].

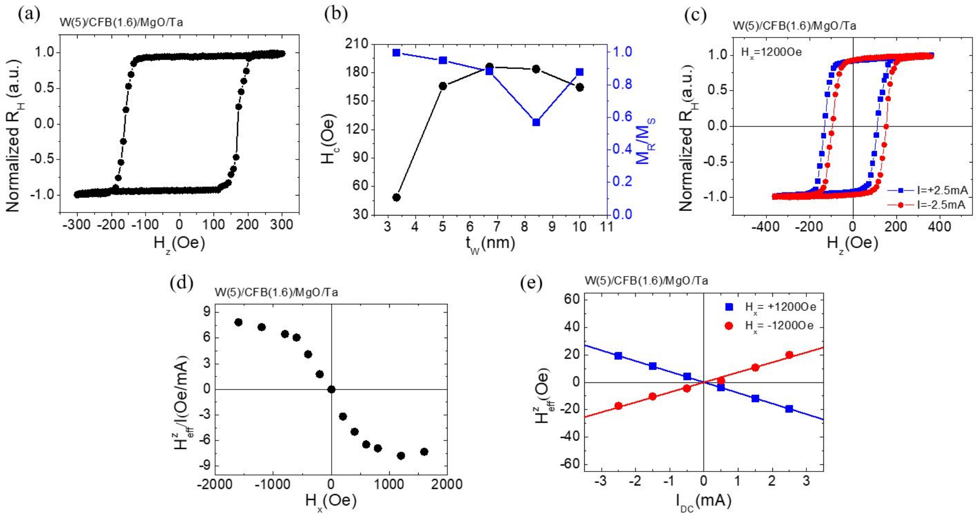

Figure 4.2: Magnetic properties and damping-like effective field characterization of W(5)/CoFeB(1.6)/MgO(1)/Ta(3) heterostructure. (a) Hystereisis loop of W(5)/CoFeB(1.6)/MgO(1)/Ta(3). (b) H_c and the remanent magnetization ratio of W(t_W)/CoFeB(1.6)/MgO(1)/Ta(3). (c) Representative hysteresis loop shift results of a W(5) based device under H_x = 1200 Oe and I_{dc} = ± 2.5mA. (d) H^z_{eff}/I as a function of H_x. (e) H^z_{eff} as a function of I_{dc} of a W(5) based device under H_x = ±1200Oe.

In order to further analyze the SOT characterization and the magnetization switching behavior of tungsten control samples, measuring Hall voltage V_H versus the out-of-plane field is necessary. Fig.4.2(a) shows the representative normalized AHE hysteresis loop of W(5)/CoFeB(1.6)/MgO(1)/Ta(3) with applied dc current 1mA. This representative sample has a sharp AHE hysteresis loop, and the coercivity field, H_c, can be obtained. The coercivity field is the strength of the magnetic field that needs to be applied in the opposite direction to demagnetize a material completely. It represents the resistance of a magnetic material to changes in its magnetization state. The value of H_c can be calculated by subtracting two out-of-plane fields as the normalized Hall voltage, R_H, equals zero. The H_c and the remanent magnetization ratio, M_R/M_S, of each sample, which indicates the PMA stability, are shown in Fig.4.2(b). After tungsten has a phase transition, which means that $t_W \geq$ 5nm, the H_c is larger than amorphous's H_c. Representative normalized AHE hysteresis loop shift results for W(5)/CoFeB(1.6)/MgO(1)/Ta(3) with H_x = 1200Oe and I_{dc} = ±2.5mA are shown in Fig.4.2(c). This shift occurs because of the existence of a current-induced effective magnetic field in the out-of-plane direction. This effective field affects the magnetization behavior under the influence of the applied current. The presence of an opposite shift in the hysteresis loop along the H_z axis, corresponding to the opposite polarity of the applied direct current, indicates the existence of the opposite direction of the effective field. Fig.4.2(d) shows that H_{eff}^z/I as a function of H_x for W(5)/CoFeB(1.6)/MgO(1)/Ta(3), and H_{eff}^z/I saturates under the large in-plane field. Fig.4.2(e) shows the relation between H_{eff}^z and I_{dc} with H_x = ±1200Oe, which can be further related to the DL efficiency.

Before discussing DL efficiency ξ_{DL}, it is important to consider another indicator called the spin Hall angle. The spin Hall angle is a characteristic of materials and de-

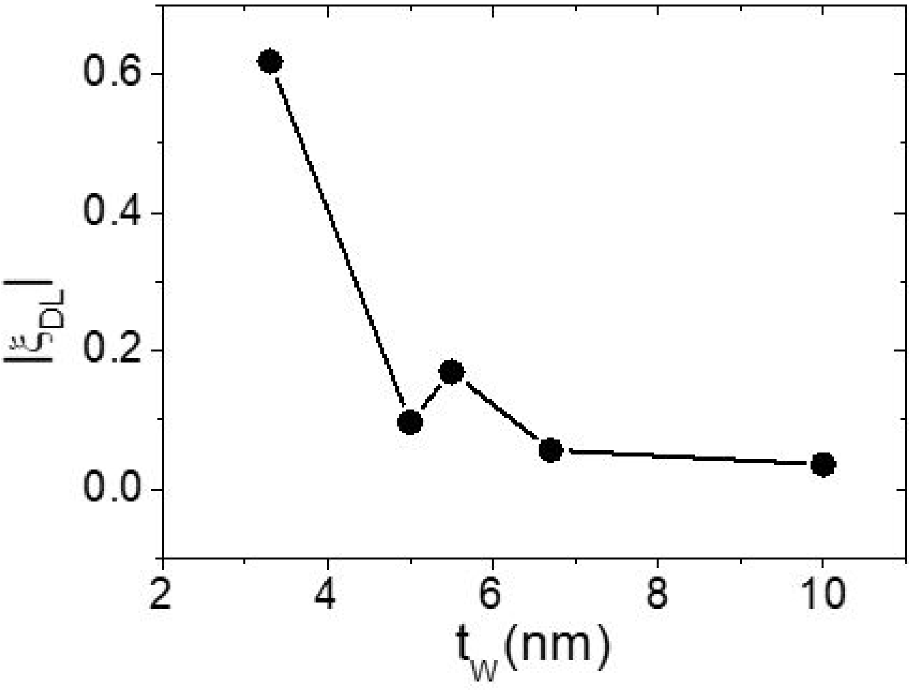

Figure 4.3: Damping-like torque efficiency characterization of W(t_W)/ CoFeB(1.6)/ MgO(1)/Ta(3).

termines the sign of the spin Hall effect. The sign of spin Hall angle differs from the material's property, for instance, platinum has a positive spin Hall angle, while tantalum and tungsten possess negative spin Hall angle[80].

As stated above, to further focus on the SOT characterization, ξ_{DL} plays a crucial role. Fig.4.3 shows the changes in $|\xi_{DL}|$ with the varieties of tungsten thickness by using equ.3.2. Because tungsten possesses a negative spin Hall angle, ξ_{DL} here is taken as the absolute value for the convenience of comparing. When $t_W = 3.3$nm, it is an amorphous structure and has a large $|\xi_{DL}|$, where $|\xi_{DL}| = 0.62$. However, if tungsten has a phase transition, $|\xi_{DL}|$ will decrease dramatically, such as $t_W = 5$nm[37, 56, 67, 80, 82, 83]. In addition, when $t_W = 3.3$nm, the spin Hall conductivity $|\sigma_{SH}^{W}| = 2.67 \times 10^5 (\hbar/2e)\Omega^{-1}m^{-1}$, while $|\sigma_{SH}^{W}| = 1.18 \times 10^5 (\hbar/2e)\Omega^{-1}m^{-1}$ as $t_W = 5$nm. The value of spin Hall conductivity can be indirectly

doi:10.6342/NTU202301664

related to the strength of SOC and SHE, and it is similar to the one in the published work with $|\sigma_{SH}^{W}| = 1.05 \times 10^5 (\hbar/2e)\Omega^{-1}m^{-1}$[67].

A material structure can be detected by several methods, such as the transmission electron microscope (TEM) and X-ray diffraction (XRD). Here, XRD analysis is conducted to detect tungsten's structure. As mentioned above, If tungsten's thickness is greater than 5nm, it will have a phase transition. Fig.4.4 has proved this statement. α-W with the BCC structure will have a peak around $2\theta = 40°$, which is tungsten's (110) plane. The peak at $2\theta = 33°$ is the signal of the silicon substrate, and it can be neglected[83, 84].

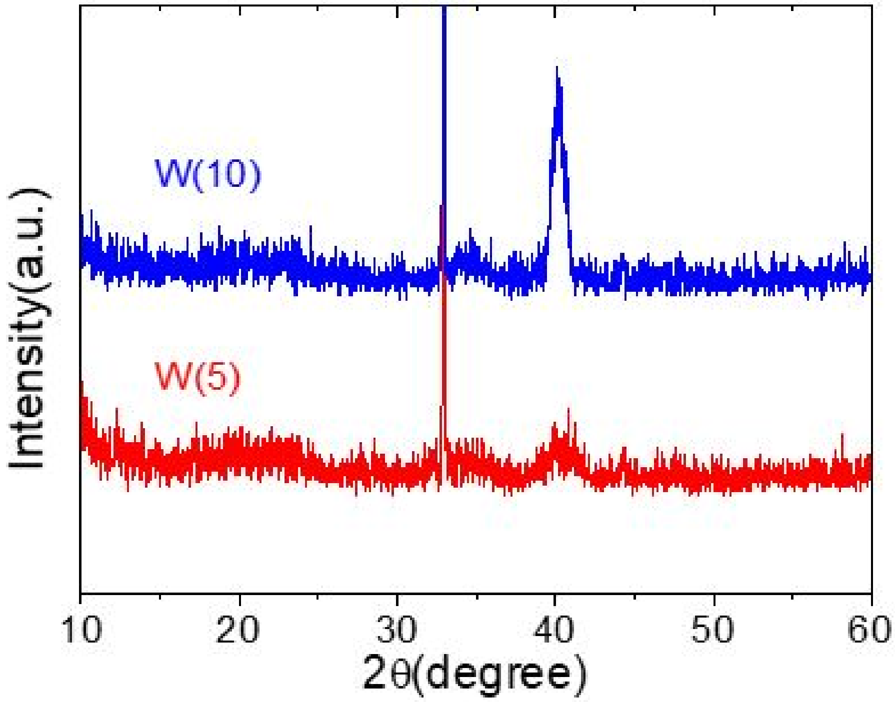

Figure 4.4: XRD results of W(5 and 10)/CoFeB(1.6)/MgO(1)/Ta(3).

Energy consumption is a crucial topic in the field of semiconductors nowadays. Finding a material with much less applied current is a priority. The representative current

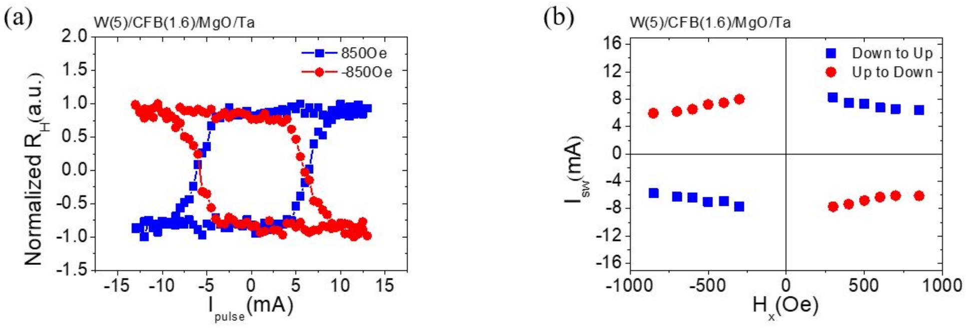

Figure 4.5: Current switching data of W(5)/CoFeB(1.6)/MgO(1)/Ta(3). (a) Representative current-induced magnetization switching loops of W(5)/CoFeB(1.6)/MgO(1)/Ta(3) with $H_\mathrm{x} = \pm 850\mathrm{Oe}$. (b) Critical switching current I_sw as a function of H_x.

switching data of W(5)/CoFeB(1.6)/MgO(1)/Ta(3) with $H_\mathrm{x} = \pm 850\mathrm{Oe}$ is shown in Fig.4.5(a). And Fig.4.5(b) shows the critical switching current I_sw and I_sw will saturate under high applied field, I_sw of W(5) is 6.45mA for instance. This value of I_sw is quite large for the SOT-MRAM, therefore, finding a brilliant material with larger DL efficiency ξ_DL and smaller switching current is necessary and it will be discussed in the following section[31, 83, 84].

4.2 SOT Characterization of WCo Alloy/CoFeB

As mentioned in the previous chapter, doping other metal elements into heavy metals is an effective method to enhance DL efficiency. This technique offers multiple benefits, for instance, it can reduce the switching current, which can save energy consumption and avoid the breakdown issue. It can also enhance DL efficiency, meaning that more spin currents are generated from the charge currents. Many previous works conduct successfully, such as PtCu alloy, WTa alloy, WV alloy, etc.[37, 42]. Although Pt-based alloys have a small switching current, which helps reduce lots of energy owing to their low resistivity. Even though there is an enhancement in the DL efficiency ξ_DL of Pt-based alloy, due to the platinum's bulk property, the DL efficiency of Pt-based alloy cannot be com-

doi:10.6342/NTU202301664

parable with tungsten. Despite numerous experiments, the improvement in DL efficiency with W-based alloys has not met expectations. Consequently, in this section, the focus will shift to using WCo alloy as the spin source for generating spin current[80, 85, 86].

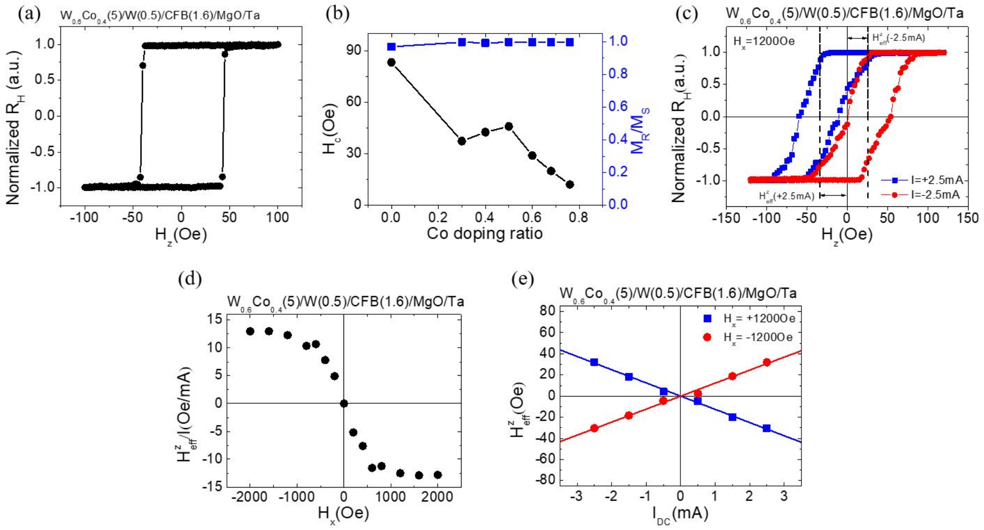

Figure 4.6: Magnetic properties and damping-like effective field characterization of $W_{0.6}Co_{0.4}$(5)/W(0.5)/CoFeB(1.6)/MgO(1)/Ta(3) heterostructure. (a) Hystereisis loop of $W_{0.6}Co_{0.4}$(5)/W(0.5)/CoFeB(1.6)/MgO(1)/Ta(3). (b) H_c and the remanent magnetization ratio of $W_{1-x}Co_x$(5)/W(0.5)/CoFeB(1.6)/MgO(1)/Ta(3). (c) Representative hysteresis loop shift results of a $W_{0.6}Co_{0.4}$(5) based device under H_x = 1200 Oe and I_{dc} = ± 2.5mA. (d) H^z_{eff}/I as a function of H_x. (e) H^z_{eff} as a function of I_{dc} of a $W_{0.6}Co_{0.4}$(5) based device under $H_x = \pm1200$Oe.

To further analyze the SOT characterization and the magnetization switching behavior of WCo alloy-based samples, a sharp hysteresis loop is necessary. Fig.4.6(a) shows the representative hysteresis loop of $W_{0.6}Co_{0.4}$(5)/W(0.5)/CoFeB(1.6)/MgO(1)/Ta(3) sample, and it has a moderate H_c and a sharp hysteresis loop. There is a 0.5nm tungsten insertion layer between WCo alloy and CoFeB. Without this insertion layer, WCo alloy/CoFeB sample cannot possess PMA property. In addition, by subtracting two fields where the magnetic states are switched, which means that the normalized R_H equals zero, H_c can be calculated. The obtained H_c and the remanent magnetization ratio M_R/M_S of $W_{1-x}Co_x$(5)/ W(0.5)/CoFeB(1.6)/MgO(1)/Ta(3) samples are shown in Fig.4.6(b). All of the samples' remanent magnetization ratios M_R/M_S are nearly one, which means that the PMA remains stable in WCo alloy-based samples. If we increase the Co doping ratio into tungsten, H_c decreases gradually because cobalt must contribute to the lattice distortion of tungsten even if annealing is conducted.

In addition, Representative normalized AHE hysteresis loop shift results for $\mathrm{W_{0.6}Co_{0.4}}$(5)/W(0.5)/CoFeB(1.6)/MgO(1)/Ta(3) with H_{x} = 1200Oe and I_{dc} = ±2.5mA are shown in Fig.4.6(c). The reason for this shift is the presence of a current-induced effective magnetic field in the out-of-plane direction. If the applied currents' directions are opposite, the directions of $H_{\mathrm{eff}}^{\mathrm{z}}$ are different. Because tungsten has a negative spin Hall angle and is still dominant in generating spin current in the WCo alloy-based samples, the loop shifts to the opposite direction compared to the direction of applied current, which means that $H_{\mathrm{eff}}^{\mathrm{z}}$ is negative under H_{x} = 1200 Oe and I_{dc} = +2.5mA, and vice versa. Fig.4.6(d) shows that $H_{\mathrm{eff}}^{\mathrm{z}}/I$ as a function of H_{x} for $\mathrm{W_{0.6}Co_{0.4}}$(5) based sample, and $H_{\mathrm{eff}}^{\mathrm{z}}/I$ saturates under the large in-plane field. The I_{dc} dependence of the measured $H_{\mathrm{eff}}^{\mathrm{z}}$ for $\mathrm{W_{0.6}Co_{0.4}}$(5)/W(0.5)/CoFeB(1.6)/MgO(1)/Ta(3) is summarized in Fig.4.6(e). The relationship between the $H_{\mathrm{eff}}^{\mathrm{z}}$ and the I_{dc} can change when the direction of the magnetic field is reversed. This behavior is in line with what is predicted by considering both the spin Hall effect, which involves the generation of spin currents due to the motion of charge carriers, and the Dzyaloshinskii-Moriya interaction (DMI) scenario, which refers to an interaction between the magnetic moments in a material that can lead to asymmetric behavior[65, 78, 80, 85, 86].

As mentioned above, a 0.5nm tungsten insertion layer is deposited between WCo alloy and CoFeB, so the equation that describes DL efficiency should be adding a correc-

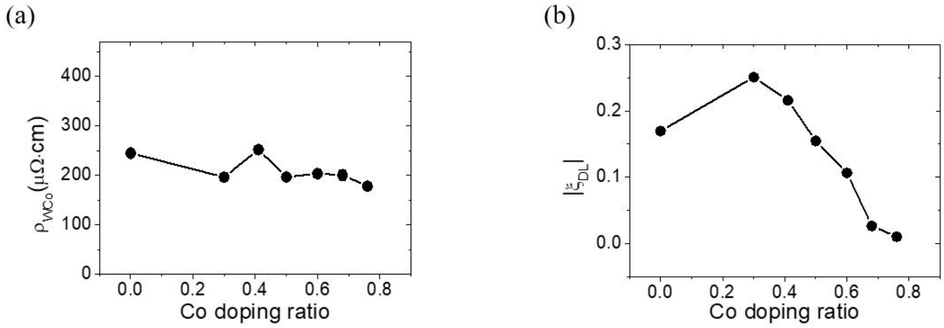

Figure 4.7: (a) Resistivity of $W_{1\text{-}x}Co_x(5)$. (b) Damping-like torque efficiency characterization of $W_{1\text{-}x}Co_x(5)/W(0.5)/CoFeB(1.6)/MgO(1)/Ta(3)$.

tion,

$$\xi_{\mathrm{DL}} = \left(\frac{2}{\pi}\right) \frac{2e}{\hbar} \mu_0 M_s t_{FM} w t_{HM} \left(1+s\right) \left(\frac{H^z_{eff}}{I}\right) \cosh\left(\frac{t_{Winsersion}}{\lambda_W}\right) \tag{4.3}$$

where λ_W is the spin diffusion length and approximately equals 1.31nm, and $t_{Winsersion}$ is the insertion layer thickness. Fig.4.7(a) shows the relation between the resistivity and the cobalt doping ratio by using equ.4.3 to calculate. With cobalt doping ratio equals zero, which means that it is pure tungsten, it has the largest resistivity. When the cobalt doping ratio increases, resistivity decreases gradually. However, it still has a large resistivity which may waste a lot of energy if it is utilized in the SOT-MRAM. Additionally, tungsten has a negative spin Hall angle, and WCo alloy-based samples as well. Therefore, the DL efficiency $|\xi_{\mathrm{DL}}|$ and cobalt doping ratio plot is shown in Fig.4.7(b). Since WCo alloy-based sample has a negative spin Hall angle, the $|\xi_{\mathrm{DL}}|$ of the WCo alloy is represented by its absolute value. This is done to facilitate convenient comparisons with other samples. Based on the figure, when the cobalt doping ratio is 0.3, it has the largest $|\xi_{\mathrm{DL}}|$ with $|\xi_{\mathrm{DL}}| =$ 0.25, which means that it can generate the most spin current among all WCo alloy-based samples. However, if we increase the cobalt doping ratio, $|\xi_{\mathrm{DL}}|$ decreases dramatically and nearly approaches to zero as the cobalt doping ratio equals 0.76. Theoretically, the conversion efficiency from the charge current to the spin current of cobalt is quite small, if a large portion of cobalt is doped into tungsten, it will make $|\xi_{\mathrm{DL}}|$ diminish dramatically even approach to zero. Unfortunately, due to the restriction of the power supply of the magnetron sputtering, it is hard to manipulate the lower doping ratio of the WCo alloy. Otherwise, based on the trend of $|\xi_{\mathrm{DL}}|$ as a function of the cobalt doping ratio, $|\xi_{\mathrm{DL}}|$ may increase by reducing the concentration of cobalt[80, 81, 85, 86]. In addition, the spin Hall conductivity $\left|\sigma_{\mathrm{SH}}^{\mathrm{WCo\ alloy}}\right| = 1.28\times10^{5}(\hbar/2e)\Omega^{-1}\mathrm{m}^{-1}$ for $\mathrm{W_{0.7}Co_{0.3}}$-based sample, while $\left|\sigma_{\mathrm{SH}}^{\mathrm{WCo\ alloy}}\right| = 5.23\times10^{4}(\hbar/2e)\Omega^{-1}\mathrm{m}^{-1}$ for $\mathrm{W_{0.4}Co_{0.6}}$-based sample. It indicates that the strength of SHE and SOC for $\mathrm{W_{0.7}Co_{0.3}}$ is greater than that of $\mathrm{W_{0.6}Co_{0.4}}$/CoFeB.

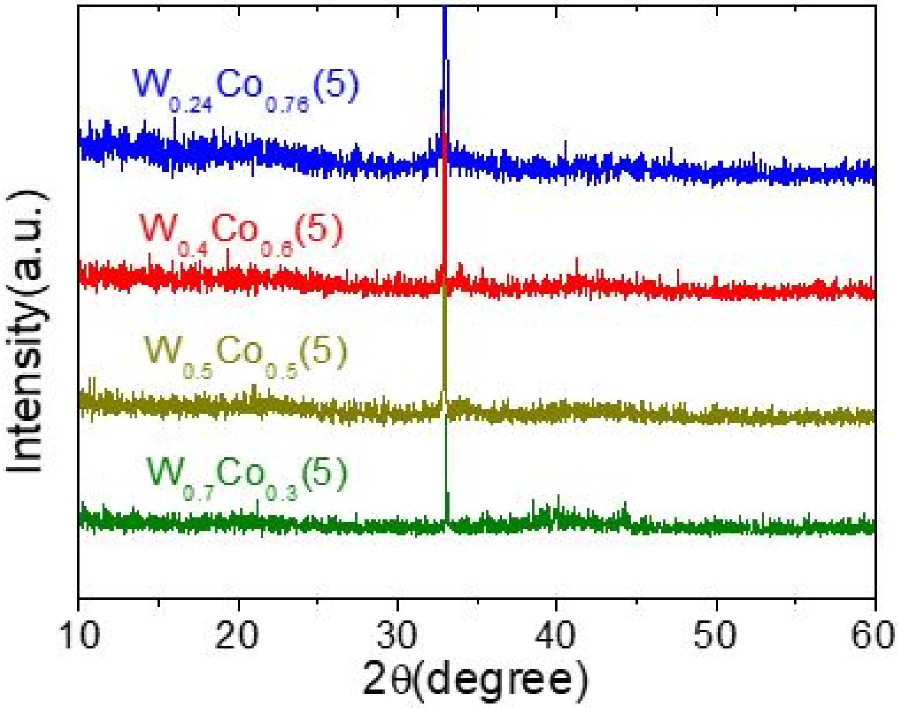

Figure 4.8: XRD results of WCo alloy(5)/W(0.5)/CoFeB(1.6)/MgO(1)/Ta(3).

After analyzing the relation between $|\xi_{\mathrm{DL}}|$ and the cobalt doping ratio, it is essential to discuss the reason why $\mathrm{W_{0.7}Co_{0.3}}$ based sample has a larger $|\xi_{\mathrm{DL}}|$ than pure tungsten's. As stated above, tungsten with t_W = 5nm is a α-W accompanied by a BCC structure. It has a (110) plane peak at $2\theta = 40°$. Additionally, as tungsten's thickness is less than 5nm, it is an amorphous structure with a larger $|\xi_{DL}|$. However, Fig.4.8 shows that all of the WCo alloys have amorphous structures, which means that if we dope cobalt into tungsten, it results in the distortion of tungsten's structure and turns the BCC structure into the amorphous structure. Therefore, $W_{0.7}Co_{0.3}$ based sample has a similar property and can generate more spin current.

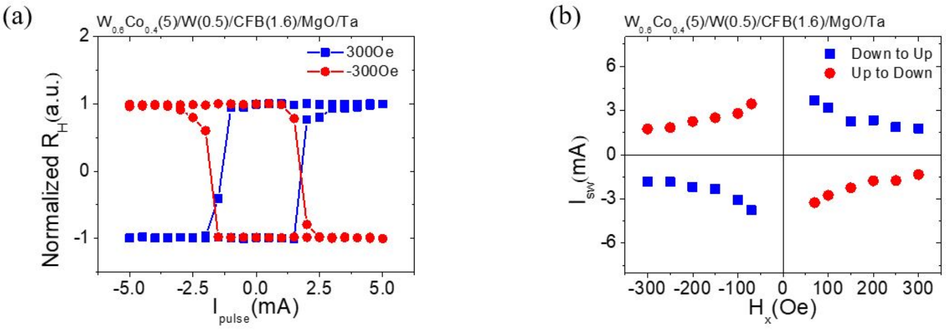

Figure 4.9: Current switching data of $W_{0.6}Co_{0.4}$(5)/W(0.5)/CoFeB(1.6)/MgO(1)/Ta(3). (a) Representative current-induced magnetization switching loops of $W_{0.6}Co_{0.4}$(5)/W(0.5)/CoFeB(1.6)/MgO(1)/Ta(3) with $H_x = \pm 300$Oe. (b) Critical switching current I_{sw} as a function of H_x of $W_{0.6}Co_{0.4}$ based sample.

The $|\xi_{DL}|$ of $W_{0.7}Co_{0.3}$ based and $W_{0.6}Co_{0.4}$ based samples are greater than tungsten's. Besides, if the switching currents of these two samples are smaller than that of pure tungsten, both of them can be considered substitutions of tungsten. Fig.4.9(a) presents the representative current-induced magnetization switching loops of $W_{0.6}Co_{0.4}$(5)/W(0.5)/CoFeB(1.6)/MgO(1)/Ta(3) under $H_x = \pm 300$Oe. The current switching loops are quite sharp, which means that the domain wall motion inside the CoFeB moves decisively. The I_{sw} versus H_x plot is shown in Fig.4.9(b). When applying a small H_x, I_{sw} tends to rise rapidly, and it approaches infinity theoretically. And if H_x is large, I_{sw} saturates to 1.78mA under $H_x = 300$Oe, which is much smaller than pure tungsten's I_{sw} ($I_{sw} = 6.45$mA under $H_x = 850$Oe)[65].

Finally, $W_{0.7}Co_{0.3}$ based and $W_{0.6}Co_{0.4}$ based samples have much smaller I_{sw} and larger value of $|\xi_{\mathrm{DL}}|$ than that of pure tungsten. Based on the trend of ξ_{DL} versus the cobalt doping ratio, $|\xi_{\mathrm{DL}}|$ may rise if reducing the cobalt concentration. However, due to the restriction of the power supply of the gun in magnetron sputtering, it is hard to develop a lower-cobalt-concentration sample. Therefore, exploring a new way that can maintain the concept of doping cobalt into tungsten and lower the cobalt doping ratio at the same time is necessary. Forming a WCo multilayer structure is an alternative method to substitute WCo alloy, and it will be discussed in the next section.

4.3 SOT Characterization of WCo Multilayer/CoFeB

In SOT-MRAM, multilayer is widely used as one of the FM layers. Compared with the single layer of CoFeB as the FM layer, using a multilayer as a FM layer such as Pt/Co/Pt multilayer has a lot of advantages. Firstly, it has a strong and stable PMA property, which can be used as a pinned layer in SOT-MRAM, and it is hard to switch its magnetic state. In addition, unlike a single layer of CoFeB, it is easy to manipulate the H_c of the multilayer, adjusting the thickness of cobalt or the amount of stacking layer of the multilayer for instance. Last but not least, there are many combinations of elements to stack the multilayer. Pt/Co, Co/Ni, Co/Pd, etc. stacking as a multilayer is commonly researched. However, there is not much work utilizing multilayer as a spin source to generate spin current. In this section, the prominent SOT characterization of WCo multilayer/CoFeB will be elaborated, for instance, high ξ_{DL} and low I_{sw}[80, 85–91].

doi:10.6342/NTU202301664

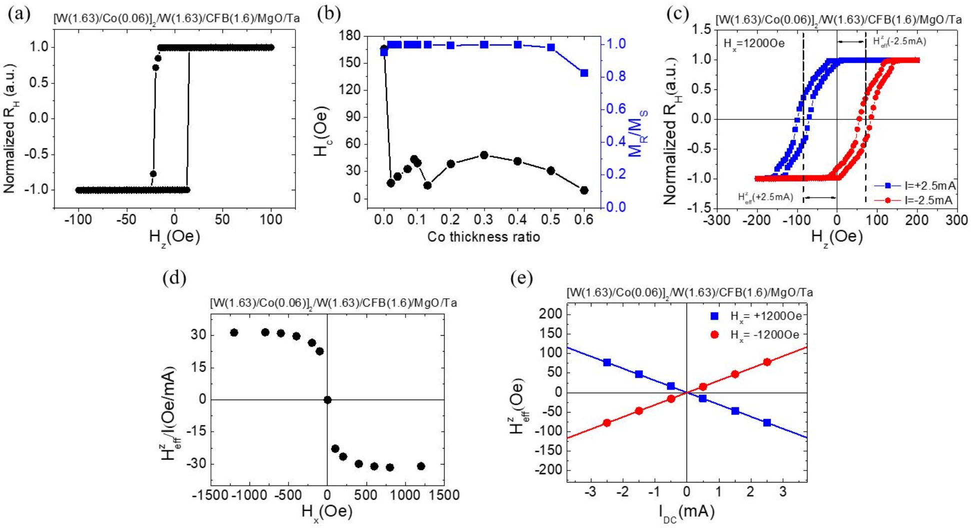

Figure 4.10: PMA properties and damping-like effective field characterization of WCo multilayer/CFB heterostructure. (a) Hysteresis loop of WCo multilayer/CFB heterostructure. (b) H_c and the remanent magnetization ratio of WCo multilayer-based samples. (c) Representative hysteresis loop shift results of a WCo multilayer/CFB heterostructure under H_x = 1200 Oe and I_dc = ± 2.5mA. (d) $H^\mathrm{z}_\mathrm{eff}/I$ as a function of H_x. (e) $H^\mathrm{z}_\mathrm{eff}$ as a function of I_dc of a representative WCo multilayer-based sample under H_x = ±1200Oe.

Fig.4.10(a) shows the representative PMA hysteresis loop of [W(1.63)/Co(0.06)]$_2$/ W(1.63) based multilayer, and the hysteresis loop is sharp, which means that the PMA property is pretty stable. By subtracting two switching fields, H_c can be obtained and is plotted in Fig.4.10(b). Also, the relation between H_c and the remanent magnetization ratio M_R/M_S and the cobalt thickness ratio is presented in Fig.4.10(b). According to the figure, all of the WCo multilayer-based devices have brilliant PMA stabilities, where $M_R/M_S \approx 1$. Besides, H_c rises first and gradually decreases when increasing the cobalt thickness ratio. Here, the representative normalized AHE hysteresis loop shift result of a [W(1.63)/Co(0.06)]$_2$/W(1.63) based multilayer with H_x = 1200 Oe and I_dc = ± 2.5mA applied is shown in Fig.4.10(c). The shift occurs because of the existence of a $H^\mathrm{z}_\mathrm{eff}$ that is generated as a result of the flowing current, and it acts in the direction perpendicular to the plane. When the currents flow in opposite directions, the resulting $H^\mathrm{z}_\mathrm{eff}$ directions also differ. It is noteworthy that WCo multilayer-based samples have negative spin Hall angles which are the same as pure tungsten's. In Fig.4.10(d), it shows the $H^\mathrm{z}_\mathrm{eff}/I$ versus H_x plot.

$H^{\mathrm{z}}_{\mathrm{eff}}/I$ still saturates at a relatively high H_{x}, and it is in line with the typical hysteresis loop shift measurement. Lastly, The dependence between the measured I_{dc} and $H^{\mathrm{z}}_{\mathrm{eff}}$ for $[\mathrm{W}(1.63)/\mathrm{Co}(0.06)]_2/\mathrm{W}(1.63)$ based multilayer is summarized in Fig.4.10(e). The sign of slope in this figure can change if adjusting H_{x} to an opposite direction, and it results from the change in direction of $H^{\mathrm{z}}_{\mathrm{eff}}$[65, 78].

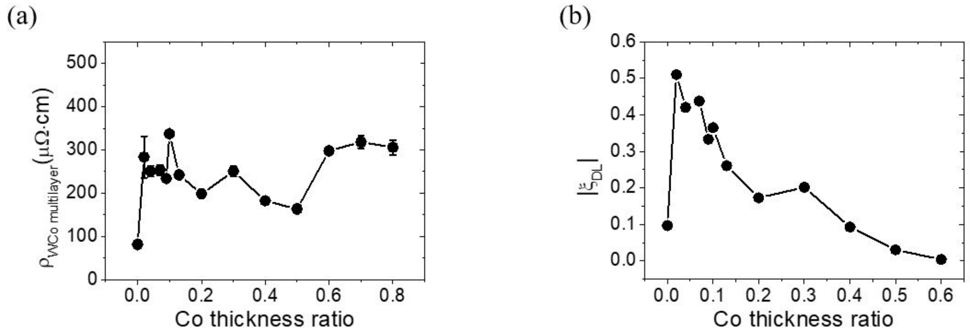

Figure 4.11: (a) Resistivity of $[\mathrm{W}(1.63)/\mathrm{Co}(0.06)]_2/\mathrm{W}(1.63)$. (b) Damping-like torque efficiency characterization of WCo multilayer/CFB heterostructure.

To further analyze the SOT characterization, resistivity should be measured first. Fig.4.11(a) shows the relation between the WCo multilayer's resistivity and the cobalt thickness ratio. For pure tungsten, it is metallic, and its resistivity is low. However, when inserting the cobalt layer into the tungsten to form a multilayer, the resistivity of the multilayer rises a lot, and it is in the range of 200 to more than 300 $\mu\Omega\cdot$cm. By applying the value of resistivity and equ.3.2, DL efficiency $|\xi_{\mathrm{DL}}|$ can be obtained and is shown in Fig.4.11(b). Because WCo multilayers have negative spin Hall angles, all of the $|\xi_{\mathrm{DL}}|$ are taken absolute values which is convenient for comparing. When the cobalt thickness ratio equals 0.02, which means that some small cobalt islands are doped on the tungsten, it has the largest $|\xi_{\mathrm{DL}}|$ and equals 0.51. Similar to the WCo alloy-based samples, if we increase the Co thickness ratio, $|\xi_{\mathrm{DL}}|$ decreases gradually and approaches zero as the Co thickness ratio = 0.6. It is important to highlight that the enhancement in $|\xi_{\mathrm{DL}}|$ is significantly higher in the case of the WCo multilayer-based sample compared to the WCo alloy-based sample, particularly when using a low cobalt doping ratio. This can be attributed to the fact that in multilayer configurations, achieving a dilute cobalt concentration is relatively simple by reducing the cobalt growth time. In contrast, for magnetron sputtering processes, it is not feasible to bombard tungsten to extremely high power while keeping cobalt at low power, as it would cause the tungsten target to melt. As mentioned earlier, this explains why the multilayer system enables higher $|\xi_{\mathrm{DL}}|$ to be achieved. After analyzing the ξ_{DL}, the value of spin Hall conductivity is calculated. The $[\mathrm{W}(1.63)/\mathrm{Co}(0.06)]_2/\mathrm{W}(1.63)/\mathrm{CoFeB}(1.6)$ attributes a value of $\left|\sigma_{\mathrm{SH}}^{\mathrm{WCo\ multilayer}}\right| = 1.80\times10^{5}(\hbar/2\mathrm{e})\Omega^{-1}\mathrm{m}^{-1}$, whereas $\left|\sigma_{\mathrm{SH}}^{\mathrm{WCo\ multilayer}}\right| = 8.04\times10^{4}(\hbar/2\mathrm{e})\Omega^{-1}\mathrm{m}^{-1}$ for $[\mathrm{W}(1.17)/\mathrm{Co}(0.75)]_2/\mathrm{W}(1.17)$-based sample.

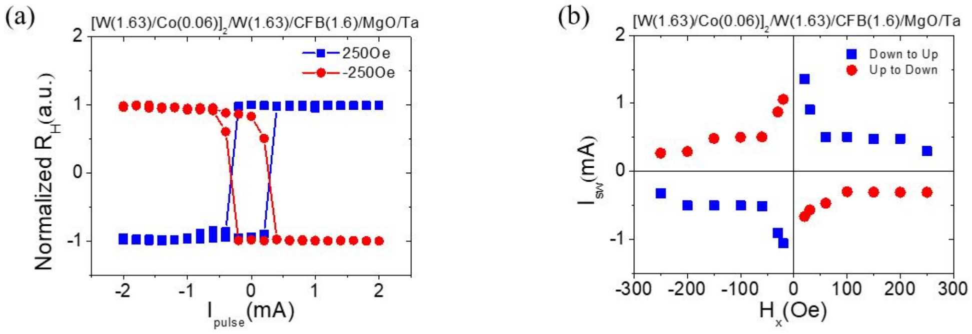

Figure 4.12: Current switching data of WCo multilayer/CFB heterostructure. (a) Representative current-induced magnetization switching loops of WCo multilayer/CFB heterostructure with $H_{\mathrm{x}} = \pm250\mathrm{Oe}$. (b) Critical switching current I_{sw} as a function of H_{x} of $[\mathrm{W}(1.63)/\mathrm{Co}(0.06)]_2/\mathrm{W}(1.63)$ based sample.

Based on the $|\xi_{\mathrm{DL}}|$ versus the cobalt thickness ratio plot mentioned above, the WCo multilayer-based samples generally have larger $|\xi_{\mathrm{DL}}|$ than pure tungsten. In addition, if the switching currents of the multilayer are smaller than that of pure tungsten, the multilayer becomes a promising alternative to replace tungsten. Here, Fig.4.12(a) shows the representative current-induced switching loops of $[\mathrm{W}(1.63)/\mathrm{Co}(0.06)]_2/\mathrm{W}(1.63)$ based sample under $H_{\mathrm{x}} = \pm250\mathrm{Oe}$. The current switching loop is sharp, so it refers to the straightforward motion of the domain wall. Also, the I_{sw} is extremely small in $[\text{W}(1.63)/\text{Co}(0.06)]_2/$ W(1.63) based multilayer under $H_{\text{x}} = \pm 250\text{Oe}$, which I_{sw} equals 0.27mA, and is shown in Fig.4.12(b). Followed by the traditional domain wall motion theory, I_{sw} under a small applied H_{x} tends to rise hastily and approach infinity[65].

4.4 Comparison between WCo Alloy/CoFeB & WCo Multilayer/CoFeB

Currently, two strategies have been explored: WCo alloy and WCo multilayer. Both of these strategies exhibit superior performance in terms of ξ_{DL} when compared to pure tungsten. Therefore, this section provides a concise comparison of the SOT characterization between the alloy and multilayer approaches.

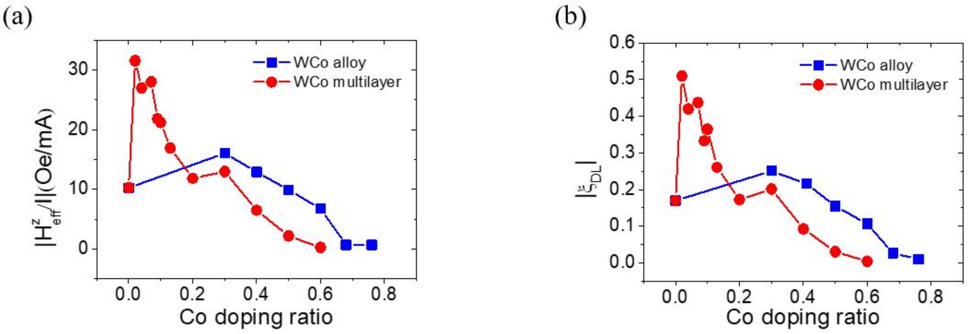

Figure 4.13: Comparison of the SOT characterization between WCo alloy-based samples and WCo multilayer-based samples. (a) the $|H^{\text{z}}_{\text{eff}}/I|$ versus the cobalt doping ratio plot. (b) the relation between $|\xi_{\text{DL}}|$ and the cobalt doping ratio.

Fig.4.13(a) displays a plotted graph that provides data on the $|H^{\text{z}}_{\text{eff}}|$ of both WCo alloy-based and WCo multilayer-based samples. For the cobalt doping ratio greater than 0.3, the $|H^{\text{z}}_{\text{eff}}|$ of alloy-based samples have a larger value than that of multilayer-based samples. However, the power supply limitations during the bombardment of the tungsten target prevent the attainment of a dilute cobalt concentration in WCo alloy-based samples, which is mentioned in the previous section. On the basis of the above, it can be concluded that only WCo multilayer-based samples can be utilized to achieve larger $|H_{\text{eff}}^{z}|$. Fig.4.13(b) illustrates the comparison between the alloy and multilayer configurations. As the $|H_{\text{eff}}^{z}|$ and $|\xi_{\text{DL}}|$ have a linear relationship based on the aforementioned equ.3.2, the $|\xi_{\text{DL}}|$ exhibits a similar trend to the $|H_{\text{eff}}^{z}|$. Furthermore, the multilayer configuration demonstrates a notable superiority in $|\xi_{\text{DL}}|$.

4.5 Adjusting Layer Repetition of WCo Multilayer/CoFeB

As stated earlier, the ξ_{DL} is significantly improved when the cobalt thickness ratio is 0.02 compared to pure tungsten. Moreover, if tungsten is in an amorphous structure, the ξ_{DL} is higher than when it is α-W[37, 56, 82, 83]. Consequently, in this section, we will focus on varying the number of layer repetitions and analyzing the SOT characterization.

Fig.4.14(a) illustrates the PMA hysteresis loop as a representative $[\text{W}(1.63)/\text{Co}(0.06)]_1/$ W(1.63)/CoFeB(1.6)/MgO(1)/Ta(3). The hysteresis loop of the multilayer with a single layer repetition demonstrates a pronounced sharpness, indicating a direct and straightforward switching of magnetic moments. By employing the aforementioned method, the coercivity field H_{c} and the remanent magnetization ratio $M_{\text{R}}/M_{\text{S}}$ are depicted in Fig.4.14(b). Across the range of one to five layers in the multilayer stack, each configuration exhibits excellent stability in terms of PMA, with the remanent magnetization ratios $M_{\text{R}}/M_{\text{S}}$ approaching unity for all cases. Nevertheless, the relationship between the H_c and the repetition of layers does not exhibit a clear pattern. This is due to the influence of the interface between the HM and FM layers. The H_c is affected by the interface, and it may not preserve the condition perfectly after the annealing process. The SOT properties were assessed using hysteresis loop shift measurements. Fig.4.14(c) displays the representative data for hysteresis loop shifts, obtained with an in-plane applied field H_x of 1200 Oe and a dc current I_{dc} of ± 2.5mA. Despite a slight distortion in the hysteresis loops under the influence of a strong H_x, the H_{eff}^z remains substantial. This further indicates significant enhancements in DL efficiencies. According to the observation in this figure, when a positive H_x and a positive I_{dc} are applied, the hysteresis loop exhibits a shift in the negative direction, indicating a negative spin Hall angle. This phenomenon is also evident in Fig.4.14(d). Similar to the statement mentioned in the previous section, the H_{eff}^z/I still continues to saturate under the influence of a strong applied field. Finally, Figure (e) presents the fitted line depicting the relationship between H_{eff}^z and I_{dc}. The variations in the direction of H_{eff}^z result in a sign change of the slope as the applied in-plane field direction is reversed[65, 78, 80].

Before calculating the ξ_{DL}, one crucial factor is missing: resistivity. By applying equ.4.2, Fig.4.15(a) showcases the resistivity of each sample, wherein the W/Co layer stacking varies. As the layer repetition increases, the resistivity of the WCo multilayer gradually decreases. Except in the case where the layer repetition equals two, the standard deviation of resistivity for each sample remains minimal. This indicates a remarkable similarity in resistivity between each device. Considering the negative spin Hall angle exhibited by the WCo multilayer-based samples, the DL efficiency is evaluated by taking

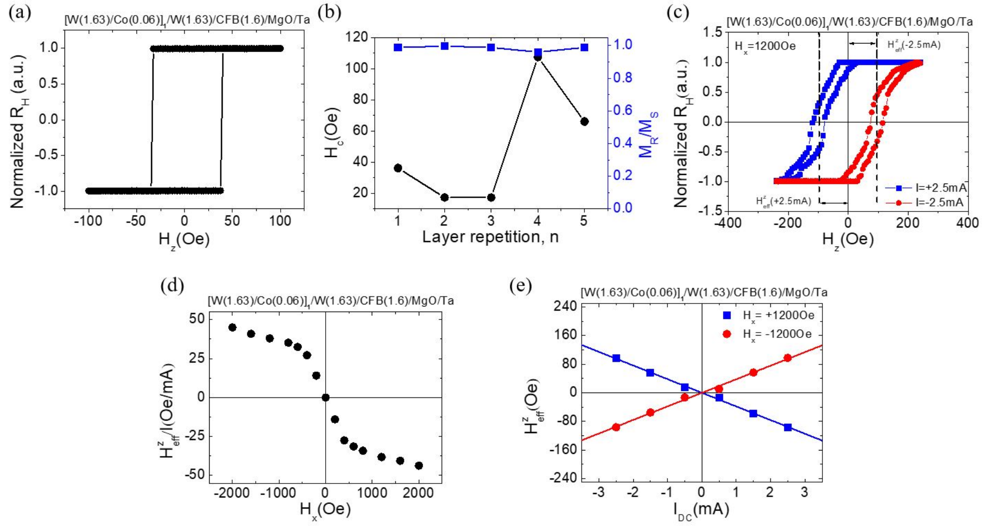

Figure 4.14: PMA properties and damping-like effective field characterization of $[\mathrm{W}(1.63)/\mathrm{Co}(0.06)]_1/\mathrm{W}(1.63)/\mathrm{CoFeB}(1.6)/\mathrm{MgO}(1)/\mathrm{Ta}(3)$ heterostructure. (a) Hystereisis loop of $[\mathrm{W}(1.63)/\mathrm{Co}(0.06)]_1/\mathrm{W}(1.63)/\mathrm{CoFeB}(1.6)/\mathrm{MgO}(1)/\mathrm{Ta}(3)$. (b) H_c and the remanent magnetization ratio of WCo multilayer-based samples. (c) Representative hysteresis loop shift results of a $[\mathrm{W}(1.63)/\mathrm{Co}(0.06)]_1/\mathrm{W}(1.63)/\mathrm{CoFeB}(1.6)/\mathrm{MgO}(1)/\mathrm{Ta}(3)$ under H_x = 1200 Oe and $I_\mathrm{dc} = \pm$ 2.5mA. (d) H^z_eff/I as a function of H_x. (e) H^z_eff as a function of I_dc of a representative WCo multilayer-based sample under $H_\mathrm{x} = \pm 1200$Oe.

its absolute value $|\xi_\mathrm{DL}|$ and is shown in Fig.4.15(b). Similar to the scenario with pure tungsten, the $|\xi_\mathrm{DL}|$ of the WCo multilayer-based sample exhibits a gradual decrease and eventually saturates at a lower value when tungsten undergoes a phase transition, forming an α-W structure. when the layer repetition is limited to one layer, the WCo multilayer-based sample achieves the highest $|\xi_\mathrm{DL}|$, reaching a value of 0.66, primarily attributed to its amorphous structure. Additionally, with one-layer stacking, the value of spin Hall conductivity is $\left|\sigma_\mathrm{SH}^\mathrm{WCo\ multilayer}\right| = 1.54\times10^5(\hbar/2\mathrm{e})\Omega^{-1}\mathrm{m}^{-1}$.

Referring to Fig.4.15, it can be observed that the $|\xi_\mathrm{DL}|$ of the WCo multilayer-based sample exhibits significant enhancement when formed by fewer than three layers, indicating the HM thickness of less than 5nm., its $|\xi_\mathrm{DL}|$ has a lot of enhancement. To analyze the underlying reasons for this phenomenon, the utilization of selected area electron diffraction (SAED) patterns through the TEM technique and XRD patterns becomes essential.

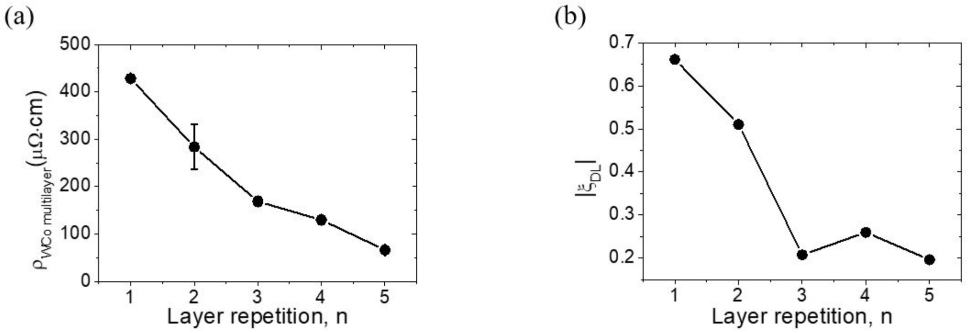

Figure 4.15: (a) Resistivity of [W(1.63)/Co(0.06)]$_1$/W(1.63). (b) Damping-like torque efficiency characterization of [W(1.63)/Co(0.06)]$_1$/W(1.63)/CoFeB(1.6)/MgO(1)/Ta(3) heterostructure.

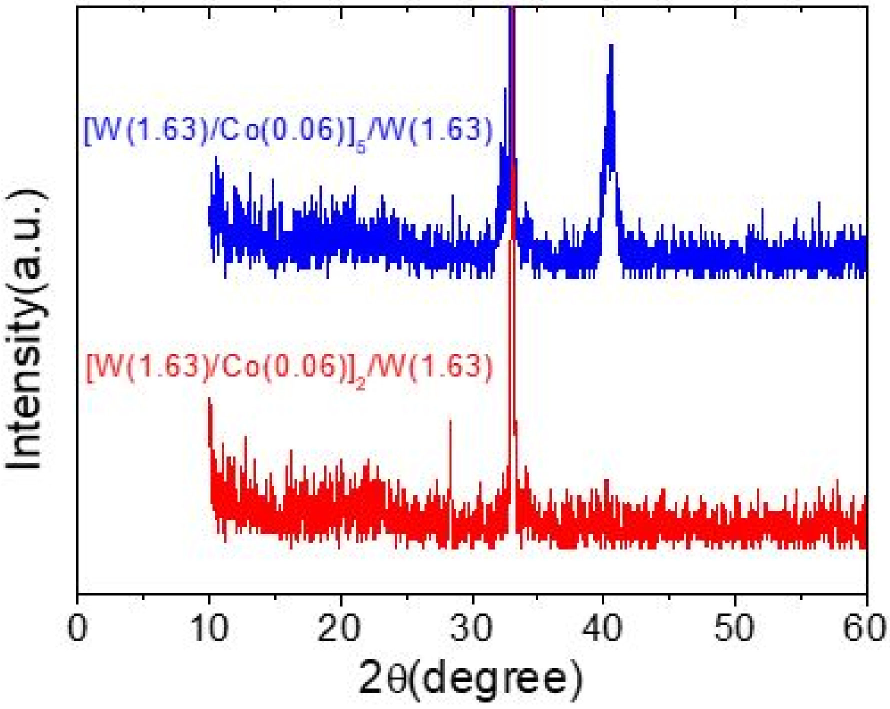

Figure 4.16: XRD results of [W(1.63)/Co(0.06)]$_2$/ W(1.63) based and [W(1.63)/Co(0.06)]$_5$/W(1.63) based heterostructure.

Utilizing the θ-2θ measurement, the XRD pattern is illustrated in Fig.4.16. When the number of layer repetitions reaches five, a distinct peak corresponding to the (110) plane of tungsten becomes evident. This indicates that the WCo multilayer adopts an α-W structure. Consequently, it is reasonable that the $|\xi_{\mathrm{DL}}|$ of this configuration is relatively low. In contrast, the $[\mathrm{W}(1.63)/\mathrm{Co}(0.06)]_2/\mathrm{W}(1.63)$ based sample exhibits an amorphous structure after eliminating the peak originating from the silicon substrate. Consequently, it is logical that this configuration displays an enhancement in $|\xi_{\mathrm{DL}}|$. The amorphous structure observed in the $[\mathrm{W}(1.63)/\mathrm{Co}(0.06)]_2/\mathrm{W}(1.63)$ based sample can be attributed to the incorporating of cobalt doping into tungsten. The presence of cobalt induces the formation of small islands, which in turn disrupts the crystalline structure of tungsten. As a consequence, the characteristic α-W structure is no longer present, leading to the amorphous nature exhibited by the sample.

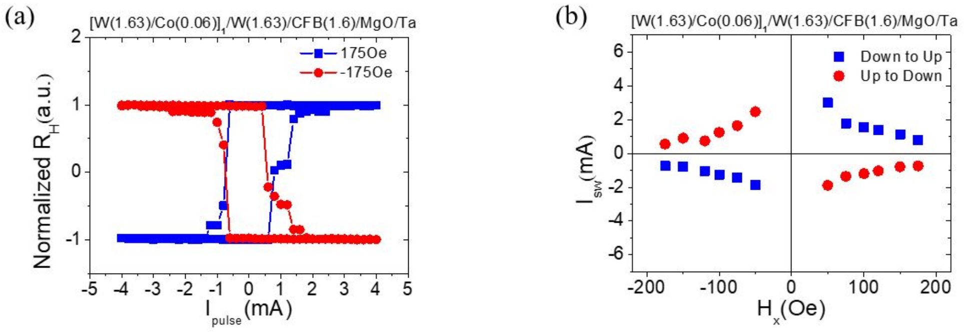

Figure 4.17: Current switching data of $[\mathrm{W}(1.63)/\mathrm{Co}(0.06)]_1$/ W(1.63)/ CoFeB(1.6)/ MgO(1)/Ta(3) heterostructure. (a) Representative current-induced magnetization switching loops of $[\mathrm{W}(1.63)/\mathrm{Co}(0.06)]_1$/W(1.63)/CoFeB(1.6)/MgO(1)/Ta(3) with $H_{\mathrm{x}} = \pm 175\mathrm{Oe}$. (b) Critical switching current I_{sw} as a function of H_{x} of $[\mathrm{W}(1.63)/\mathrm{Co}(0.06)]_1/\mathrm{W}(1.63)$ based sample.

As previously discussed, the $[\mathrm{W}(1.63)/\mathrm{Co}(0.06)]_1$/W(1.63)/CoFeB(1.6)/MgO(1)/Ta(3) configuration demonstrates the largest $|\xi_{\mathrm{DL}}|$. However, before considering its use as a spin current source in SOT-MRAM, it is important to evaluate the switching current[31, 85, 86]. A low switching current is desirable as it enables the substitution of pure tungsten, resulting in avoiding the breakdown issue. Therefore, an examination of the switching current is necessary before its potential application in the SOT-MRAM. Fig.4.17(a) illustrates the representative current-induced magnetization switching loops of $[W(1.63)/Co(0.06)]_1/W(1.63)$ based sample, with an applied in-plane field of $H_x = \pm 175$Oe. The corresponding switching currents under various in-plane fields are plotted in Fig.4.17(b). It is worth mentioning that when a relatively high value of H_x is applied, the switching current reaches an extremely low saturation point. Specifically, at $H_x = 175$Oe, the I_{sw} drops to a remarkably small value of 0.79mA. This exceptionally low I_{sw} presents a substantial opportunity for energy conservation when utilized as a spin source in SOT-MRAM. Additionally, it demonstrates a satisfactory $|\xi_{DL}|$, indicating an efficient conversion from charge currents to spin currents[80, 85, 86].

4.6 Thickness Issue between W/CoFeB Control Sample & WCo Multilayer/CoFeB

Currently, the reduction of the cobalt doping ratio in WCo alloy-based samples is challenging due to limitations in magnetron sputtering techniques. Moreover, the WCo multilayer configuration is the only viable option to meet the desired objectives. Therefore, the previous section showcases the results obtained by modifying the layer repetition in the WCo multilayer. In this context, a comparison is conducted between the variation in the HM thickness for the W/CoFeB control samples and the WCo multilayer/CoFeB samples.

doi:10.6342/NTU202301664

As mentioned earlier, due to the negative spin Hall angle, the values of H^z_{eff}/I and ξ_{DL} are presented in their absolute form. Fig.4.18(a) shows a comparison of $|H^z_{\text{eff}}/I|$ between W-based control samples and the WCo multilayer-based samples under different HM thickness. It is observed that the WCo multilayer/CoFeB samples exhibit an enhancement in $|H^z_{\text{eff}}/I|$ for every HM thickness. Notably, the largest enhancement occurs when the HM thickness is 5nm. The trends of $|\xi_{\text{DL}}|$ are illustrated in Fig.4.18(b), showing a similar pattern to $|H^z_{\text{eff}}/I|$. It is worth noting that the largest improvement in $|\xi_{\text{DL}}|$ is observed when the HM thickness is 5nm compared to other HM thickness values, showing a difference of approximately 0.56. In contrast to the 5nm thickness of the tungsten layer in the control sample with a BCC structure, the enhancement in $|\xi_{\text{DL}}|$ can be attributed to the amorphous structure of the WCo multilayer with the HM thickness of 5nm, as observed in the XRD patterns shown in Fig.4.16. This amorphous structure facilitates a notable enhancement in $|\xi_{\text{DL}}|$. In addition, it can be found that the WCo multilayer/CoFeB samples consistently demonstrate an increase in $|\xi_{\text{DL}}|$ across all variations of HM thickness[80].

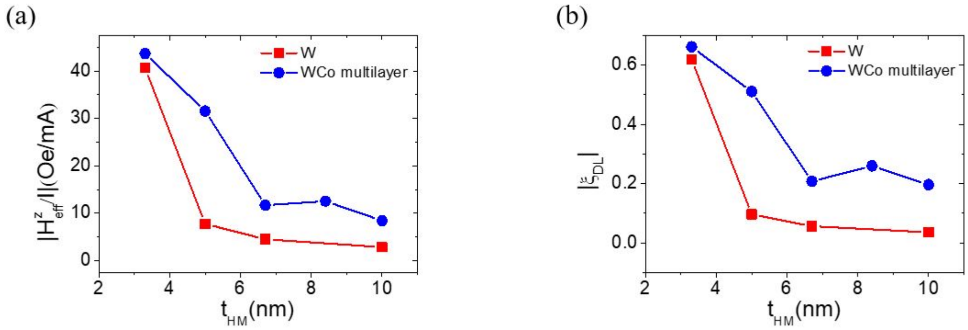

Figure 4.18: Comparison of the SOT characterization between W-based samples and WCo multilayer-based samples. (a) the $|H^z_{\text{eff}}/I|$ versus the HM thickness plot. (b) the relation between $|\xi_{\text{DL}}|$ and the HM thickness.

4.7 Short Summary

Over the past few decades, tungsten has been extensively studied and utilized in SOT-MRAM applications. While tungsten exhibits a significant ξ_{DL} compared to other heavy metals, it is associated with relatively high switching currents. Therefore, it is imperative to explore alternative materials that can serve as a replacement for pure tungsten, offering both high ξ_{DL} and low energy consumption.

Referring to the moderate ξ_{DL} of W/CoFeB and the observed improvement in ξ_{DL} with alloy-based HM/FM heterostructures, the use of WCo alloy/CoFeB is being considered. Among the various cobalt doping ratios tested, the alloy with a cobalt doping ratio of 0.3 demonstrates the highest $|\xi_{\mathrm{DL}}|$, and it decreases as the cobalt doping ratio is increased. The XRD analysis of the WCo alloys demonstrates the amorphous structure of the alloys as well. However, due to the limitations and constraints of the magnetron sputtering machine, it is not feasible to deposit an alloy with a cobalt doping ratio lower than 0.3. As a result, taking inspiration from the work executed by other research groups, we shift our focus to the WCo multilayer/CoFeB configurations.

To deposit a WCo multilayer, the process involves initially growing a layer of tungsten and then adding a layer of cobalt on top. This sequence is repeated multiple times. It is possible to significantly decrease the thickness ratio of cobalt by depositing it for just a few seconds. Based on the results of hysteresis loop-shift measurement and the ξ_{DL}, it was found that the WCo multilayer/CoFeB heterostructure exhibits the highest $|\xi_{\mathrm{DL}}|$ with a value of 0.51 when the cobalt thickness ratio is 0.02. At a thickness of 5nm for the HM

doi:10.6342/NTU202301664

layer, the ξ_{DL} is remarkably high. However, as the thickness ratio of cobalt increases, the $|\xi_{\mathrm{DL}}|$ gradually decreases. Furthermore, when the ratio is set to 0.02, the I_{sw} associated with the WCo multilayer is significantly small, measuring only 0.27mA. This observation highlights the exceptional spin characteristics of the WCo multilayer, making it a promising alternative to pure tungsten in SOT-MRAM applications[65, 78].

Given the outstanding performance of the WCo multilayer with a cobalt thickness ratio of 0.02, it becomes meaningful to explore variations in the number of stacking layers. The findings indicate that a single layer stacking exhibits the highest $|\xi_{\mathrm{DL}}|$, reaching a value of 0.66. However, when considering the improvement in $|\xi_{\mathrm{DL}}|$ compared to the pure tungsten control samples, the largest enhancement is observed with a two-layer repetition, where the HM layer is 5nm in thickness. Based on the XRD data analysis, it was observed that under a constant HM thickness of 5nm, pure tungsten exhibits a BCC crystal structure. On the other hand, the WCo multilayer shows an amorphous structure. This distinction in crystal structures contributes to the notable enhancement in ξ_{DL} achieved by the WCo multilayer[92].

doi:10.6342/NTU202301664

Chapter 5 Spin-Orbit Torque Characterizations of WTi Multilayer

Based on the previous chapter, it was observed that the WCo multilayer exhibits both a high DL efficiency and a low switching current. A significant DL efficiency indicates a strong ability to convert charge currents into spin currents, which can produce torque and reverse the direction of magnetic moments. On the other hand, a small switching current contributes to a small applied voltage, preventing the breakdown issue, which is a prior issue nowadays[31]. Taking a leaf out of WCo multilayer's book, this chapter focuses on analyzing the SOT characterization by introducing titanium, another 3d transition metal, into the tungsten to form a multilayer[93].

5.1 SOT Characterization of WTi Multilayer/CoFeB

Titanium, like cobalt, belongs to the 3d transition metal group and is widely utilized in diverse industries due to its advantageous characteristics. Furthermore, titanium can be obtained through the refinement of various minerals and is considered a relatively abun-

doi:10.6342/NTU202301664

dant natural resource. Taking inspiration from the remarkable performance of the WCo multilayer, therefore, the following section focuses on elaborating on the SOT characterization of the WTi multilayer/CoFeB.

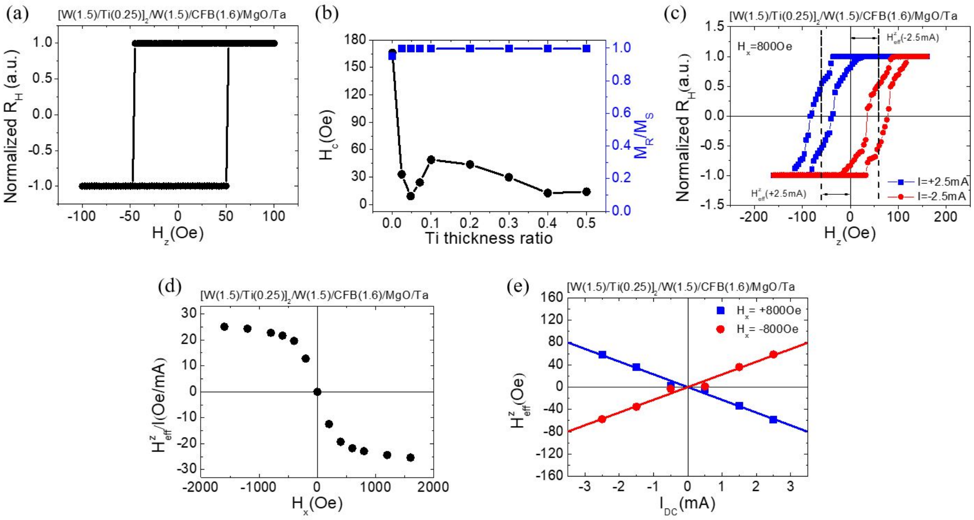

Figure 5.1: PMA properties and damping-like effective field characterization of WTi multilayer heterostructure. (a) Hystereisis loop of WTi multilayer heterostructure. (b) H_c and the remanent magnetization ratio of WTi multilayer-based samples. (c) Representative hysteresis loop shift results of a WTi multilayer heterostructure under H_x = 800 Oe and I_{dc} = ± 2.5mA. (d) H^z_{eff}/I as a function of H_x. (e) H^z_{eff} as a function of I_{dc} of a representative WTi multilayer-based sample under H_x = ±800Oe.

We employed the same technique used for the WCo multilayer/CoFeB case to investigate the SOT properties of the WTi multilayer/CoFeB system. To analyze the SOT characteristics, we utilized a current-induced hysteresis loop shift measurement. Fig.5.1(a) displays the typical data of the hysteresis loop for the WTi multilayer heterostructure. The hysteresis loop exhibits a moderate H_c and demonstrates clear and distinct switching behavior. By subtracting the two switching fields, we were able to calculate the H_c for each titanium thickness ratio, as illustrated in Fig.5.1(b). Furthermore, the figure also displays the remanent magnetization ratio, M_R/M_S. Interestingly, regardless of the titanium thickness ratio, the M_R/M_S ratio remains at unity, indicating that all the samples with WTi multilayer-based HM layer exhibit strong PMA stability.

Furthermore, in order to analyze the DL torque, H_{eff}^{z} should be examined first. Fig.5.1(c) presents the representative hysteresis loop shift results, which are indicative of H_{eff}^{z}. From the figure, it is observed that when a positive in-plane field is applied along with a positive dc current, the hysteresis loop shifts in the opposite direction compared to the H_{x} direction. This indicates that H_{eff}^{z} points towards the negative z direction, resulting in the motion of domain walls. As a result, the domain wall migrates to an opposite direction compared to a positive spin Hall angle's element does, platinum for instance. This indicates that the WTi multilayer exhibits a negative spin Hall angle, which is similar to the behavior observed in the WCo multilayer. Fig.5.1(d) depicts the relation between H_{eff}^{z}/I and H_{x}. H_{eff}^{z}/I reaches saturation at a relatively high in-plane field and decreases as H_{x} is reduced. This behavior aligns with the conventional scenario observed in hysteresis loop shift measurements. A linear fitting of the slope of H_{eff}^{z} with respect to I_{dc} is performed under $H_{\mathrm{x}} = \pm 800\mathrm{Oe}$, as illustrated in Fig.5.1(e). It is observed that H_{eff}^{z} points to an opposite direction when the direction of the in-plane field is reversed.

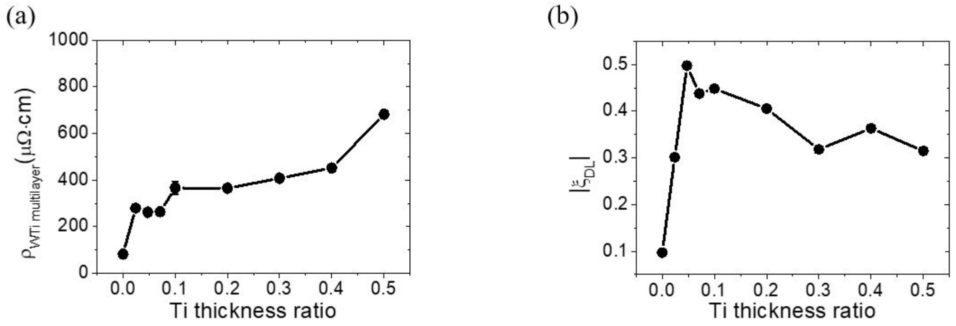

Figure 5.2: (a) Resistivity of WTi multilayer. (b) Damping-like torque efficiency characterization of WTi multilayer heterostructure.

Before delving into the analysis of the DL efficiency ξ_{DL}, it is crucial to measure the resistivity. Fig.5.2(a) displays the relation between the resistivity of the WTi multilayer and the titanium thickness ratio. Pure tungsten exhibits a metallic property; however, even a small amount of titanium doping into tungsten causes an increase in resistivity. Furthermore, as the titanium thickness ratio is increased, the resistivity gradually rises at a slower pace. Using the measured resistivity value and equ.3.2, The value of ξ_{DL} can be calculated. Since the WTi multilayer/CoFeB demonstrates a negative spin Hall angle, we consider the absolute value of ξ_{DL}, and it is depicted in Fig.5.2(b). During the magnetron sputtering process, titanium is deposited at a power of 100 Watts. When the titanium thickness ratio is 0.024, the corresponding deposition time for titanium is only a second. For a titanium thickness ratio of 0.047, the corresponding deposition time of titanium increases to two seconds. However, due to the limited deposition time for the 0.024 thickness ratio, its $|\xi_{\mathrm{DL}}|$ does not reach the maximum value. Instead, the largest $|\xi_{\mathrm{DL}}|$ is achieved at a titanium thickness ratio of 0.047, where $|\xi_{\mathrm{DL}}| = 0.5$. In the meantime, as the titanium thickness ratio decreases, $|\xi_{\mathrm{DL}}|$ gradually drops as well. Moreover, It is observed that a sample with a titanium thickness ratio of 0.047 has a large spin Hall conductivity with the value of $\left|\sigma_{\mathrm{SH}}^{\mathrm{WTi\ multilayer}}\right| = 1.90\times10^5(\hbar/2e)\Omega^{-1}\mathrm{m}^{-1}$.

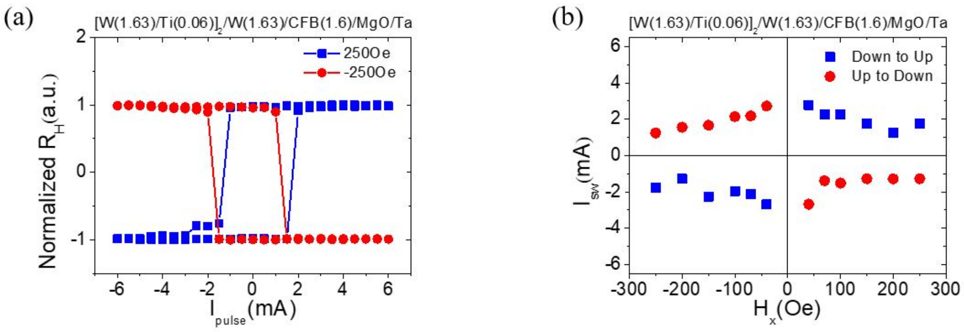

Figure 5.3: Current switching data of WTi multilayer heterostructure. (a) Representative current-induced magnetization switching loops of WTi multilayer heterostructure with H_{x} = ±250Oe. (b) Critical switching current I_{sw} as a function of H_{x} of WTi multilayer-based sample.

In addition, the current-induced SOT magnetization switching is highly significant.

Fig.5.3(a) presents the representative data showcasing the switching behavior under H_x = $\pm$250Oe, it is observed that the magnetization can be completely switched by a dc current. By subtracting the two switching currents, we obtain the relationship between I_sw and H_x, as illustrated in Fig.5.3(b). It is noteworthy that I_sw saturates around H_x = 200Oe, and its magnitude is remarkably small, with a value of 0.15mA. This combination of a small saturation field, low I_sw and moderate ξ_DL holds potential advantages for the application of the SOT-MRAM.

5.2 Adjusting Layer Repetition of WTi Multilayer/CoFeB

In the previous section, a recipe for achieving a WTi multilayer with a moderate DL efficiency and a low switching current has been discussed. Drawing on the findings from the layer repetition study of the WCo multilayer in the previous chapter, it was observed that the largest $|\xi_\mathrm{DL}|$ value was obtained with a single layer stacking, while the largest enhancement in ξ_DL was observed with two layers stacking. In this section, the impact of varying stacking layers on the SOT characterization is explored, aiming to further enhance its performance.

Fig.5.4(a) shows the AHE hysteresis loop of $[\mathrm{W}(1.59)/\mathrm{Ti}(0.12)]_1$/W(1.59)/CoFeB(1.6)/MgO(1)/Ta(3) heterostructure. The hysteresis loop exhibits a sharp switching behavior with a moderate H_c. The H_c and remanent magnetization ratio M_R/M_S with different layer repetitions is depicted in Fig.5.4(b). Notably, the M_R/M_S value remains unity for each layer repetition, indicating the presence of excellent PMA stability in the WTi multilayer-based samples. Fig.5.4(c) displays the representative hysteresis loop shift results under $H_x = 800$ Oe and $I_{dc} = \pm 2.5$mA. The observed shift in the hysteresis loop corresponds to the H^z_{eff}, which is shown in Fig.5.4(d) as a typical loop shift data. Fig.5.4(e) presents the slope between H^z_{eff} and the I_{dc} of the $[W(1.59)/Ti(0.12)]_1$/W(1.59)/CoFeB(1.6)/MgO(1)/Ta(3) heterostructure.

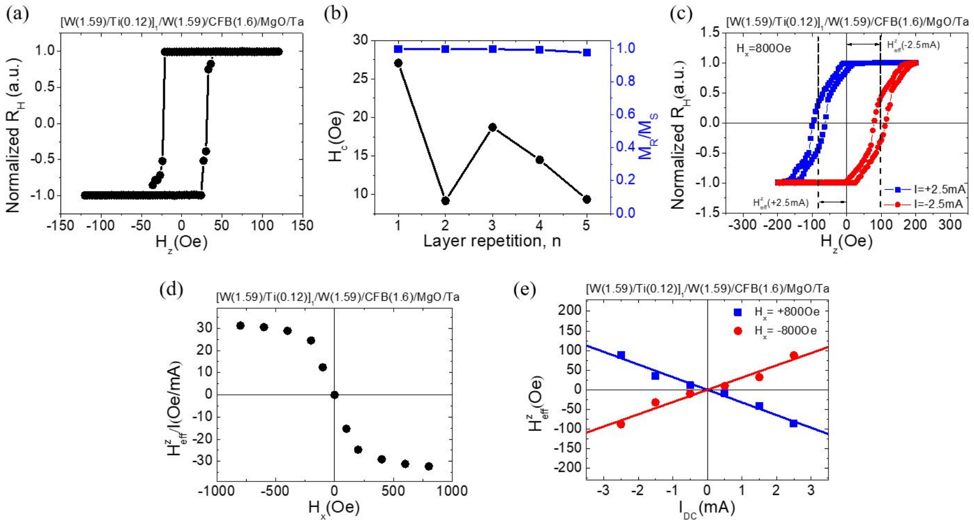

Figure 5.4: PMA properties and damping-like effective field characterization of one-layer WTi multilayer heterostructure. (a) Hysteresis loop of one-layer WTi multilayer heterostructure. (b) H_c and the remanent magnetization ratio of WTi multilayer-based samples. (c) Representative hysteresis loop shift results of a one-layer WTi multilayer heterostructure under $H_x = 800$ Oe and $I_{dc} = \pm 2.5$mA. (d) H^z_{eff}/I as a function of H_x. (e) H^z_{eff} as a function of I_{dc} of a representative WTi multilayer-based sample under $H_x = \pm 800$Oe.

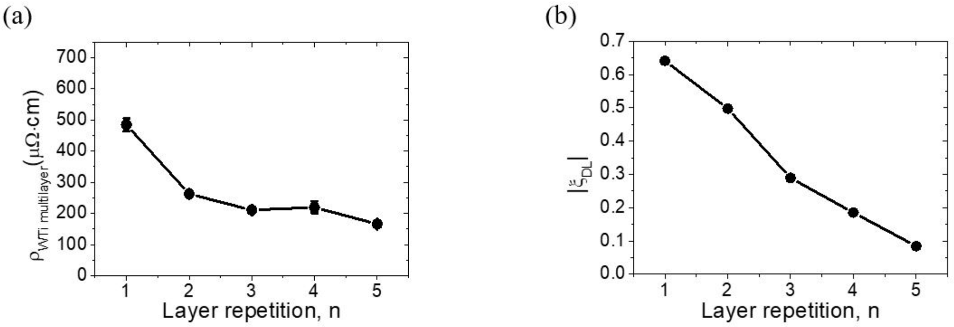

Figure 5.5: (a) Resistivity of $[W(1.59)/Ti(0.12)]_1$/W(1.59). (b) Damping-like torque efficiency characterization of one-layer WTi multilayer heterostructure.

Furthermore, in order to analyze the DL efficiency, it is necessary to calculate the resistivity first. Adopting equ.4.2, the WTi multilayer's resistivity is obtained and shown in Fig.5.5(a). It can be observed that with a single layer stacking, the WTi multilayer exhibits the highest resistivity, with a value of $\rho_{\mathrm{WTi\ multilayer}} = 484.8\mu\Omega\cdot\mathrm{cm}$. In addition, as the layer repetition increases, the resistivity significantly decreases due to the increased thickness of tungsten layers. By substituting the values of H^{z}_{eff}/I and $\rho_{\mathrm{WTi\ multilayer}}$ into equ.3.2, ξ_{DL} can be calculated. Since the WTi multilayer/CoFeB exhibits a negative spin Hall angle, the absolute value of ξ_{DL} is taken into consideration. Fig.5.5(b) shows the relation between $|\xi_{\mathrm{DL}}|$ and the layer repetition. Similar to the WCo multilayer/CoFeB, with a single layer stacking, the WTi multilayer/CoFeB achieves the highest $|\xi_{\mathrm{DL}}|$ value, reaching $|\xi_{\mathrm{DL}}| = 0.64$. However, as the number of stacking layers increases, $|\xi_{\mathrm{DL}}|$ gradually decreases. Furthermore, with a single layer stacking, the spin Hall conductivity $\left|\sigma_{\mathrm{SH}}^{\mathrm{WTi\ multilayer}}\right| = 1.32\times10^{5}(\hbar/2e)\Omega^{-1}\mathrm{m}^{-1}$.

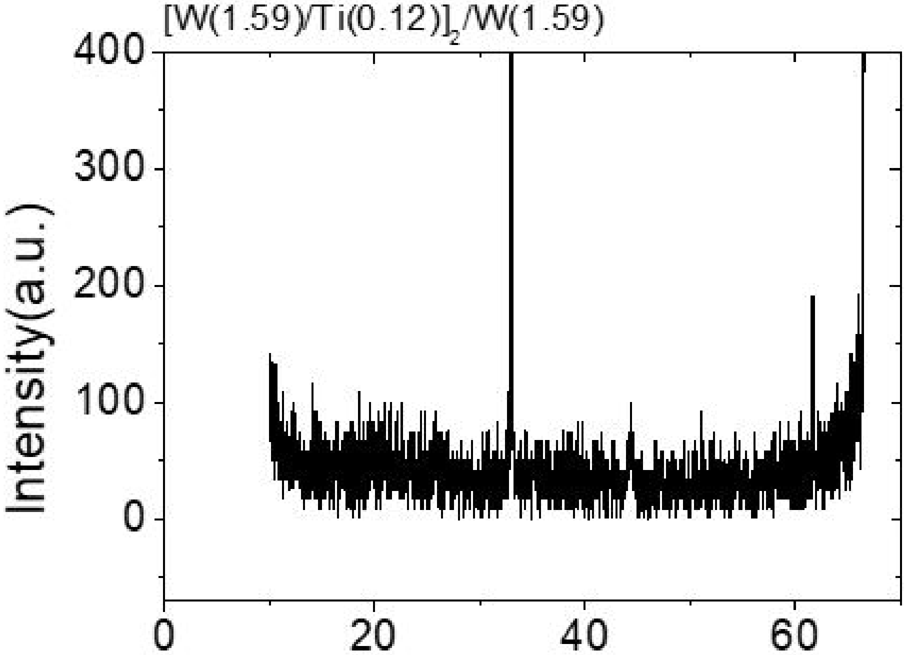

Figure 5.6: XRD result of WTi multilayer-based heterostructure.

It is noteworthy that even with two stacking layer repetitions, where the thickness of the HM layer is 5nm, the WTi multilayer/CoFeB still exhibits a moderate value of $|\xi_{\mathrm{DL}}|$. This behavior can be attributed to the findings presented in Fig.5.6. Compared to a pure tungsten layer with t_{W} = 5nm, where a BCC (110) plane peak is observed at around 2θ = 40°, and the $[\mathrm{W}(1.59)/\mathrm{Ti}(0.12)]_2/\mathrm{W}(1.59)$ based sample reveals an amorphous structure. This amorphous structure contributes to the moderate value of $|\xi_{\mathrm{DL}}|$ observed in Fig.5.5(b).

As mentioned above, the WTi multilayer/CoFeB sample exhibits a high DL efficiency with a value of $|\xi_{\mathrm{DL}}| = 0.64$. Furthermore, it demonstrates a low switching current, making it a promising candidate as a replacement for the HM layer in the SOT-MRAM applications. Fig.5.7(a) shows the current-induced switching loop data, indicating that the magnetic moment undergoes a complete and decisive switching. Fig.5.7(b) illustrates the variation of I_{sw} with different applied H_{x}. Notably, at H_{x} = 250Oe, the corresponding I_{sw} value is 0.16mA, which is the smallest I_{sw} observed in this work.

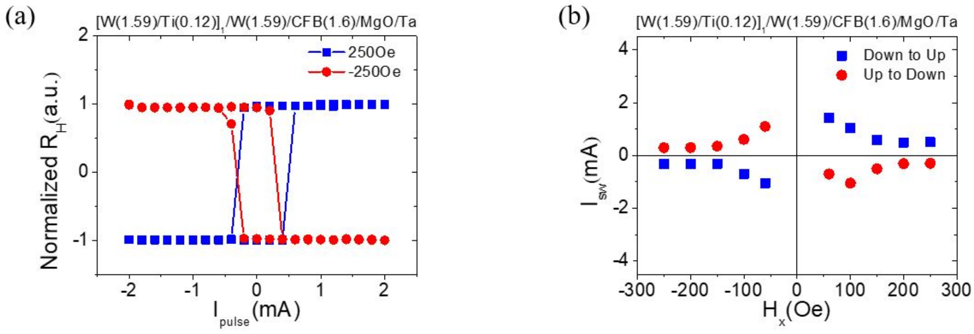

Figure 5.7: Current switching data of one-layer WTi multilayer heterostructure. (a) Representative current-induced magnetization switching loops of $[\mathrm{W}(1.59)/\mathrm{Ti}(0.12)]_1/\mathrm{W}(1.59)/\mathrm{CoFeB}(1.6)/\mathrm{MgO}(1)/\mathrm{Ta}(3)$ with $H_{\mathrm{x}} = \pm 250$e. (b) Critical switching current I_{sw} as a function of H_{x} of $[\mathrm{W}(1.59)/\mathrm{Ti}(0.12)]_1/\mathrm{W}(1.59)$ based sample.

5.3 Comparison between WCo Multilayer/CoFeB & WTi Multilayer/CoFeB

At this stage, two types of multilayers have been discussed: the WCo multilayer and the WTi multilayer. Both of them have moderate ξ_{DL} values and small I_{sw} magnitudes, making them suitable as a HM layer for the spin current generation and for reducing power consumption, respectively. In this section, a comparison between these two multilayers is conducted.

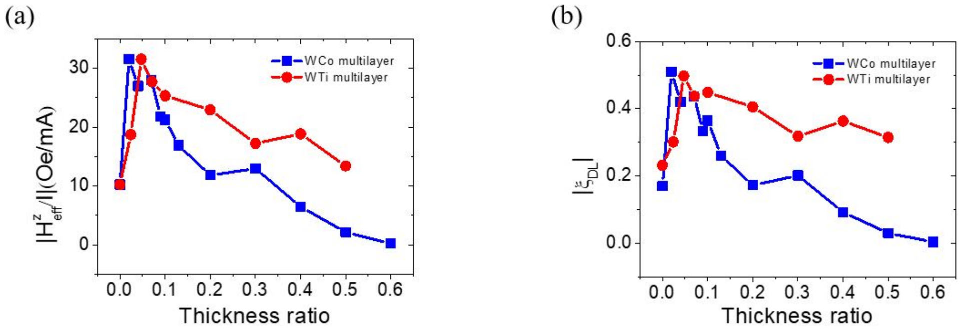

Figure 5.8: Comparison of the SOT characterization between WCo multilayer-based samples and WTi multilayer-based samples. (a) the $|H^z_{\mathrm{eff}}/I|$ versus the thickness ratio plot. (b) the relation between $|\xi_{\mathrm{DL}}|$ and the thickness ratio.

Fig.5.8(a) shows the trend of $|H^z_{\mathrm{eff}}/I|$ with varying thickness ratios. It can be observed that both the WCo multilayer/CoFeB and the WTi multilayer/CoFeB exhibit similar maximum values. As the thickness ratio increases, the $|H^z_{\mathrm{eff}}/I|$ value decreases for both multilayers. However, the WTi multilayer demonstrates superior performance in this regard. The relation between $|\xi_{\mathrm{DL}}|$ and the thickness ratio is demonstrated in Fig.5.8(b) to characterize the damping-like (DL) torque. Once again, both the WCo multilayer/CoFeB and the WTi multilayer/CoFeB display similar maximum $|\xi_{\mathrm{DL}}|$ values. However, in this case, the WCo multilayer exhibits a relatively larger $|\xi_{\mathrm{DL}}|$ value of 0.51, whereas the WTi multilayer's $|\xi_{\mathrm{DL}}|$ is 0.5 at a thickness ratio of 0.047. Also, Additionally, as the thickness ratio increases, the $|\xi_{\mathrm{DL}}|$ value decreases for both multilayers. Nevertheless, the WTi multilayer continues to demonstrate superior performance in this regard.

5.4 Thickness Issue between W/CoFeB Control Sample, WCo Multilayer/CoFeB & WTi Multilayer/CoFeB

In the previous section, the properties of SOT for different thickness ratios have been examined. It was observed that both the WCo multilayer and WTi multilayer exhibit excellent behavior at low thickness ratios. Consequently, this section will delve into the topic of thickness variation.

Fig.5.9(a) illustrates the variation in the $|H^z_{\mathrm{eff}}/I|$, as the thickness of the HM layer changes. It can be observed that the values decrease as the t_{HM} increases. Fig.5.9(b) depicts the relationship between ξ_{DL} and the HM thickness.At a thickness of t_{HM} = 3.3nm, all samples exhibit similar $|\xi_{\mathrm{DL}}|$ values. The WCo multilayer demonstrates a relatively high $|\xi_{\mathrm{DL}}|$ value, followed by the WTi multilayer. It is noteworthy that when t_{HM} = 5nm, both the WCo multilayer and WTi multilayer display moderate $|\xi_{\mathrm{DL}}|$ values of 0.51 and 0.5, respectively. These values are significantly higher than the pure tungsten's value of 0.09. Furthermore, as the HM layer thickness continues to increase, the $|\xi_{\mathrm{DL}}|$ values of the WCo multilayer and WTi multilayer gradually decrease. Fig.5.9(c-d) display the current-induced switching data of the WCo multilayer and WTi multilayer, respectively, which is discussed in the following figure.

doi:10.6342/NTU202301664

Fig.5.10 shows the switching current I_{sw} for each HM layer at a fixed layer thickness of 5 nm. The pure tungsten/CoFeB exhibits the highest I_{sw} value of 6.45mA. On the other hand, the WCo multilayer and WTi multilayer demonstrate the lowest I_{sw} values. The I_{sw} of the WCo multilayer equals 0.27mA, which reduces 95.8% compared to the pure tungsten case. Meanwhile, the WTi multilayer has a value of 0.16mA, which reduces 97.5% compared to the pure tungsten/CoFeB.

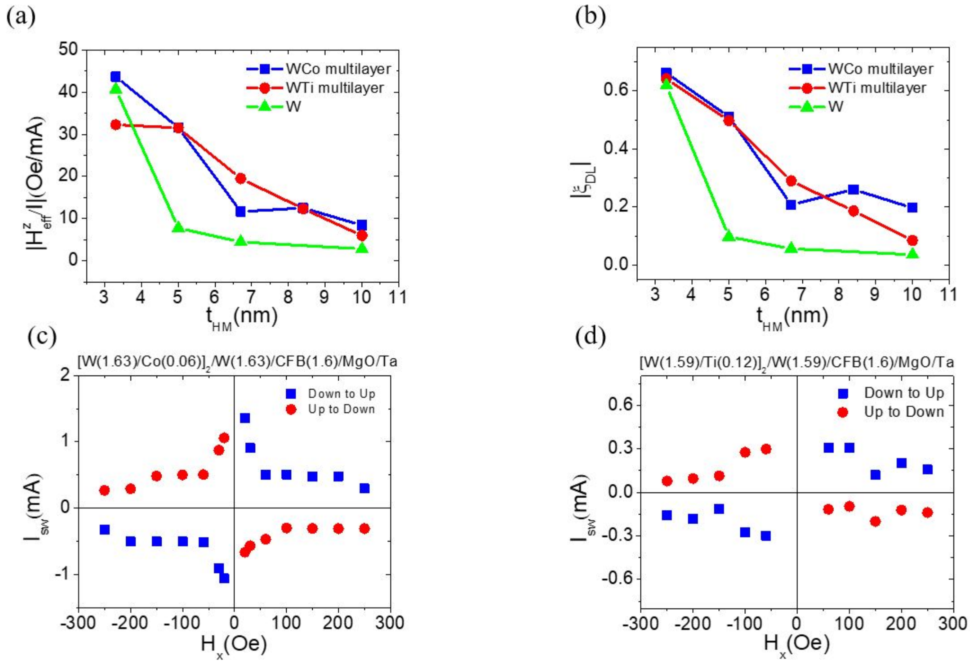

Figure 5.9: Comparison of the SOT characterization between tungsten control samples, WCo multilayer-based samples, and WTi multilayer-based samples. (a) the $|H^{z}_{\mathrm{eff}}/I|$ versus the HM layer thickness plot. (b) the relation between $|\xi_{\mathrm{DL}}|$ and the HM layer thickness. (c) Representative current switching data of $[\mathrm{W}(1.63)/\mathrm{Co}(0.06)]_2$/W(1.63)/CoFeB(1.6)/MgO(1)/Ta(3). (d) Critical switching current I_{sw} data of $[\mathrm{W}(1.59)/\mathrm{Ti}(0.12)]_2$/W(1.59) based sample.

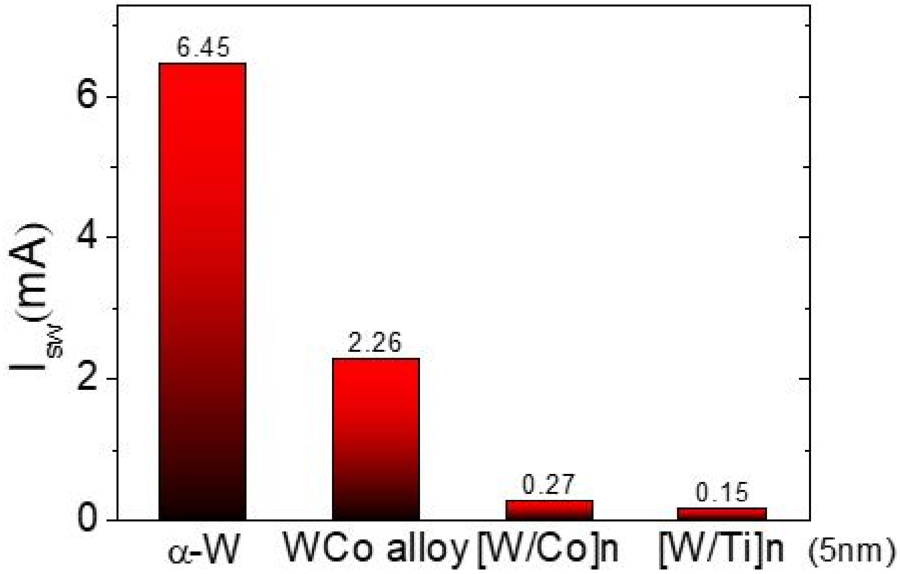

Figure 5.10: The I_{sw} comparison at a fixed thickness with t_{HM} = 5nm.

doi:10.6342/NTU202301664

Chapter 6 Summary

In SOT-MRAM, pure tungsten has traditionally been utilized as the HM layer to generate spin currents. Amorphous-structure tungsten exhibits moderate ξ_{DL} but a relatively high resistivity. This high resistivity gives rise to the thermal effect, which results in additional effects in SOT characterization and leads to an increase in power consumption. Therefore, a material with a high ξ_{DL}, a moderate resistivity and low I_{sw} has a potential for the HM layer to prevent the breakdown issue, reducing power consumption and improving overall performance. At this stage, three substitutions of pure tungsten as a HM layer to generate spin current have been introduced: WCo alloy, WCo multilayer, and WTi layer.

$\mathrm{W_{0.7}Co_{0.3}}$(5)/CoFeB(1.6) performs a normal ξ_{DL} with an absolute value of $|\xi_{\mathrm{DL}}| = 0.25$, and its switching current I_{sw} equals 2.26mA. The trend of $|\xi_{\mathrm{DL}}|$ with varying cobalt doping ratio indicates a decrease in $|\xi_{\mathrm{DL}}|$ as the cobalt doping ratio increases. However, due to the limitations and restrictions of the magnetron sputtering machine, it is not feasible to deposit tungsten using high-power bombardment. As a result, the deposition of WCo alloy with low cobalt concentration cannot be achieved.

Considering the inconvenience associated with the WCo alloy, the WCo multilayer is being considered as an alternative HM layer. Among the various WCo multilayers tested, the $[\mathrm{W}(1.63)/\mathrm{Co}(0.06)]_2/\mathrm{W}(1.63)/\mathrm{CoFeB}(1.6)$ heterostructure demonstrates the best performance. It exhibits a moderate $|\xi_{\mathrm{DL}}|$ with the value of 0.51, while maintaining a low I_{sw} of 0.27 mA. Furthermore, as the cobalt thickness ratio is increased, there is a gradual decrease in $|\xi_{\mathrm{DL}}|$.

Referring to a brilliant performance done by the WCo multilayer, subsequent investigations were carried out on the WTi multilayer. Utilizing high-power titanium deposition, $[\mathrm{W}(1.59)/\mathrm{Ti}(0.12)]_2/\mathrm{W}(1.59)/\mathrm{CoFeB}(1.6)$ demonstrates the most promising SOT properties. It shows a moderate ξ_{DL}, where $|\xi_{\mathrm{DL}}| = 0.5$, while having a low value of I_{sw} of 0.16 mA. Furthermore, similar to the trend observed in the WCo multilayer, there was a gradual decrease in $|\xi_{\mathrm{DL}}|$ as the titanium thickness ratio increased.

Given the high ξ_{DL} exhibited in amorphous-structure tungsten, it is crucial to explore the impact of layer repetition on enhancing SOT characterization. The stacking layer configuration was examined, ranging from one layer to five layers, for both the WCo multilayer and the WTi multilayer. Focusing on the representative SOT property, ξ_{DL}, it was observed that both the WCo multilayer and the WTi multilayer achieved their highest ξ_{DL} values with a single layer stacking, measuring at 0.66 and 0.64, respectively. However, the significant difference in ξ_{DL} compared to pure tungsten does not manifest with a single-layer stacking. Instead, the most remarkable enhancement in ξ_{DL} occurs when there are two layers in repetition. Notably, the XRD data indicate that pure tungsten exhibits a BCC structure when $t_{\mathrm{W}} = 5$nm. However, both the WCo multilayer and the WTi multilayer display amorphous structures under $t_{\mathrm{HM}} = 5$nm.

doi:10.6342/NTU202301664

In a nutshell, when considering a single-layer repetition, $[\mathrm{W}(1.63)/\mathrm{Co}(0.06)]_1/\mathrm{W}(1.63)/\mathrm{CoFeB}(1.6)$ and $[\mathrm{W}(1.59)/\mathrm{Ti}(0.12)]_1/\mathrm{W}(1.59)/\mathrm{CoFeB}(1.6)$ exhibit outstanding performance in terms of SOT characterization. Moreover, both of them with two-layer stacking demonstrate a remarkable improvement in ξ_{DL} compared to pure tungsten. In addition, both the WCo multilayer and WTi multilayer showcase an exceptionally low I_{sw}. having the potential to maintain the yield during the production process of the devices, especially in the etching process.

References

[1] K v Klitzing, Gerhard Dorda, and Michael Pepper. New method for high-accuracy determination of the fine-structure constant based on quantized hall resistance. Physical review letters, 45(6):494, 1980.

[2] Robert B Laughlin. Anomalous quantum hall effect: an incompressible quantum fluid with fractionally charged excitations. Physical Review Letters, 50(18):1395, 1983.

[3] Markus Konig, Steffen Wiedmann, Christoph Brune, Andreas Roth, Hartmut Buhmann, Laurens W Molenkamp, Xiao-Liang Qi, and Shou-Cheng Zhang. Quantum spin hall insulator state in hgte quantum wells. Science, 318(5851):766–770, 2007.

[4] Cui-Zu Chang and Mingda Li. Quantum anomalous hall effect in time-reversal-symmetry breaking topological insulators. Journal of Physics: Condensed Matter, 28(12):123002, 2016.

[5] Edwin H Hall et al. On a new action of the magnet on electric currents. American Journal of Mathematics, 2(3):287–292, 1879.

[6] Robert Karplus and JM Luttinger. Hall effect in ferromagnetics. Physical Review, 95(5):1154, 1954.

[7] NA Sinitsyn. Semiclassical theories of the anomalous hall effect. Journal of Physics: Condensed Matter, 20(2):023201, 2007.

[8] Naoto Nagaosa, Jairo Sinova, Shigeki Onoda, Allan H MacDonald, and Nai Phuan Ong. Anomalous hall effect. Reviews of modern physics, 82(2):1539, 2010.

[9] NA Sinitsyn, AH MacDonald, T Jungwirth, VK Dugaev, and Jairo Sinova. Anomalous hall effect in a two-dimensional dirac band: The link between the kubo-streda formula and the semiclassical boltzmann equation approach. Physical Review B, 75(4):045315, 2007.

[10] T Jungwirth, Qian Niu, and AH MacDonald. Anomalous hall effect in ferromagnetic semiconductors. Physical review letters, 88(20):207208, 2002.

[11] Masaru Onoda and Naoto Nagaosa. Topological nature of anomalous hall effect in ferromagnets. Journal of the Physical Society of Japan, 71(1):19–22, 2002.

[12] Ming-Che Chang and Qian Niu. Berry phase, hyperorbits, and the hofstadter spectrum: Semiclassical dynamics in magnetic bloch bands. Physical Review B, 53(11):7010, 1996.

[13] Ganesh Sundaram and Qian Niu. Wave-packet dynamics in slowly perturbed crystals: Gradient corrections and berry-phase effects. Physical Review B, 59(23):14915, 1999.

[14] Luc Berger. Side-jump mechanism for the hall effect of ferromagnets. Physical Review B, 2(11):4559, 1970.

[15] Ph Nozieres and CJJPF Lewiner. A simple theory of the anomalous hall effect in semiconductors. Journal de Physique, 34(10):901–915, 1973.

doi:10.6342/NTU202301664

[16] J Smit. The spontaneous hall effect in ferromagnetics i. Physica, 21(6-10):877–887, 1955.

[17] Jan Smit. The spontaneous hall effect in ferromagnetics ii. Physica, 24(1-5):39–51, 1958.

[18] Axel Hoffmann. Spin hall effects in metals. IEEE transactions on magnetics, 49(10):5172–5193, 2013.

[19] JE Hirsch. Spin hall effect. Physical review letters, 83(9):1834, 1999.

[20] Jairo Sinova, Sergio O Valenzuela, Jörg Wunderlich, CH Back, and T Jungwirth. Spin hall effects. Reviews of modern physics, 87(4):1213, 2015.

[21] Can O Avci. Current-induced effects in ferromagnetic heterostructures due to spin-orbit coupling. PhD thesis, ETH Zurich, 2015.

[22] Yuichiro K Kato, Roberto C Myers, Arthur C Gossard, and David D Awschalom. Observation of the spin hall effect in semiconductors. science, 306(5703):1910–1913, 2004.

[23] G Vignale. Ten years of spin hall effect. Journal of superconductivity and novel magnetism, 23:3–10, 2010.

[24] John Schliemann. Spin hall effect. International Journal of Modern Physics B, 20(09):1015–1036, 2006.

[25] Tomas Jungwirth, Jörg Wunderlich, and Kamil Olejník. Spin hall effect devices. Nature materials, 11(5):382–390, 2012.

[26] Hiroshi Kontani, T Tanaka, DS Hirashima, K Yamada, and J Inoue. Giant orbital hall effect in transition metals: Origin of large spin and anomalous hall effects. Physical review letters, 102(1):016601, 2009.

[27] Yasutomo Omori, Edurne Sagasta, Yasuhiro Niimi, Martin Gradhand, Luis E Hueso, Felix Casanova, and YoshiChika Otani. Relation between spin hall effect and anomalous hall effect in 3 d ferromagnetic metals. Physical Review B, 99(1):014403, 2019.

[28] Shigeki Onoda, Naoyuki Sugimoto, and Naoto Nagaosa. Quantum transport theory of anomalous electric, thermoelectric, and thermal hall effects in ferromagnets. Physical review B, 77(16):165103, 2008.

[29] Pietro Gambardella. Introduction to spin torques and spin-orbit torques in metal layers. Spinmechanics III, 87, 2015.

[30] Ioan Mihai Miron, Kevin Garello, Gilles Gaudin, Pierre-Jean Zermatten, Marius V Costache, Stéphane Auffret, Sébastien Bandiera, Bernard Rodmacq, Alain Schuhl, and Pietro Gambardella. Perpendicular switching of a single ferromagnetic layer induced by in-plane current injection. Nature, 476(7359):189–193, 2011.

[31] Luqiao Liu, Chi-Feng Pai, Y Li, HW Tseng, DC Ralph, and RA Buhrman. Spin-torque switching with the giant spin hall effect of tantalum. Science, 336(6081):555–558, 2012.

[32] Luqiao Liu, Takahiro Moriyama, DC Ralph, and RA Buhrman. Spin-torque ferromagnetic resonance induced by the spin hall effect. Physical review letters, 106(3):036601, 2011.

[33] Arne Brataas, Andrew D Kent, and Hideo Ohno. Current-induced torques in magnetic materials. Nature materials, 11(5):372–381, 2012.

[34] Yumeng Yang, Hang Xie, Yanjun Xu, Ziyan Luo, and Yihong Wu. Multistate magnetization switching driven by spin current from a ferromagnetic layer. Physical Review Applied, 13(3):034072, 2020.

[35] Noriyuki Sato, Gary A Allen, William P Benson, Benjamin Buford, Atreyee Chakraborty, Michael Christenson, Tanay A Gosavi, Philip E Heil, Nafees A Kabir, Brian J Krist, et al. Cmos compatible process integration of sot-mram with heavy-metal bi-layer bottom electrode and 10ns field-free sot switching with stt assist. In 2020 IEEE Symposium on VLSI Technology, pages 1–2. IEEE, 2020.

[36] Rajagopalan Ramaswamy, Yi Wang, Mehrdad Elyasi, M Motapothula, T Venkatesan, Xuepeng Qiu, and Hyunsoo Yang. Extrinsic spin hall effect in cu 1- x pt x. Physical Review Applied, 8(2):024034, 2017.

[37] Chen-Yu Hu and Chi-Feng Pai. Benchmarking of spin–orbit torque switching efficiency in pt alloys. Advanced Quantum Technologies, 3(8):2000024, 2020.

[38] Lijun Zhu, Daniel C Ralph, and Robert A Buhrman. Highly efficient spin-current generation by the spin hall effect in au 1- x pt x. Physical Review Applied, 10(3):031001, 2018.

[39] Minh-Hai Nguyen, Mengnan Zhao, Daniel C Ralph, and Robert A Buhrman. Enhanced spin hall ratios by al and hf impurities in pt thin films. Bulletin of the American Physical Society, 61, 2016.

[40] Zelalem Abebe Bekele, Xionghua Liu, Yi Cao, and Kaiyou Wang. High-efficiency spin–orbit torque switching using a single heavy-metal alloy with opposite spin hall angles. Advanced Electronic Materials, 7(1):2000793, 2021.

[41] Katharina Fritz, Sebastian Wimmer, Hubert Ebert, and Markus Meinert. Large spin hall effect in an amorphous binary alloy. Physical Review B, 98(9):094433, 2018.

[42] Yong Jin Kim In Ho Cha Taehyun Kim Min Hyeok Lee OukJae Lee Hionsuck Baik Soon Cheol Hong Sonny H. Rhim Gyu Won Kim, Do Duc Cuong and Young Keun Kim. Spin–orbit torque engineering in β-w/cofeb heterostructures with w–ta or w–v alloy layers between β-w and cofeb. NPG Asia Materials, 13(1):60, 2021.

[43] D Qu, SY Huang, GY Guo, and CL Chien. Inverse spin hall effect in a u x t a 1- x alloy films. Physical Review B, 97(2):024402, 2018.

[44] Tian-Yue Chen, Chun-Te Wu, Hung-Wei Yen, and Chi-Feng Pai. Tunable spin-orbit torque in cu-ta binary alloy heterostructures. Physical Review B, 96(10):104434, 2017.

[45] Jun Wu, Lvkuan Zou, Tao Wang, Yunpeng Chen, Jianwang Cai, Jun Hu, and John Q Xiao. Spin hall angle and spin diffusion length in au–cu alloy. IEEE Transactions on Magnetics, 52(7):1–4, 2016.

[46] Chi-Feng Pai and Denny D Tang. MAGNETIC MEMORY TECHNOLOGY: Spin-transfer-torque Mram and Beyond. John Wiley & Sons, 2020.

[47] I Safi. Recent aspects concerning dc reactive magnetron sputtering of thin films: a review. Surface and Coatings Technology, 127(2-3):203–218, 2000.

[48] Jon Tomas Gudmundsson. Physics and technology of magnetron sputtering discharges. Plasma Sources Science and Technology, 29(11):113001, 2020.

[49] Deok Jung Kim, WG Oldham, and AR Neureuther. Development of positive photoresist. IEEE Transactions on Electron Devices, 31(12):1730–1736, 1984.

doi:10.6342/NTU202301664

[50] Hyung Suk Lee and Jun-Bo Yoon. A simple and effective lift-off with positive photoresist. Journal of Micromechanics and Microengineering, 15(11):2136, 2005.

[51] Makoto Hanabata, Yasunori Uetani, and Akihiro Furuta. Design concept for a high-performance positive photoresist. Journal of Vacuum Science & Technology B: Microelectronics Processing and Phenomena, 7(4):640–650, 1989.

[52] Peter J Wasilewski. Magnetic hysteresis in natural materials. Earth and Planetary Science Letters, 20(1):67–72, 1973.

[53] HWF Sung and C Rudowicz. Physics behind the magnetic hysteresis loop—a survey of misconceptions in magnetism literature. Journal of magnetism and magnetic materials, 260(1-2):250–260, 2003.

[54] L Tauxe, TAT Mullender, and T Pick. Potbellies, wasp-waists, and superparamagnetism in magnetic hysteresis. Journal of Geophysical Research: Solid Earth, 101(B1):571–583, 1996.

[55] Madan Rao, HR Krishnamurthy, and Rahul Pandit. Magnetic hysteresis in two model spin systems. Physical Review B, 42(1):856, 1990.

[56] Carina Belvin Luis Henrique Vilela-Leão D. C. Ralph Chi-Feng Pai, Minh-Hai Nguyen and R. A. Buhrman. Enhancement of perpendicular magnetic anisotropy and transmission of spin-hall-effect-induced spin currents by a hf spacer layer in w/hf/cofeb/mgo layer structures. Applied Physics Letters, 104(8):082407, 2014.

[57] Paul Kinsler. Faraday’s law and magnetic induction: Cause and effect. 2019.

[58] Lowell T Wood, Ray M Rottmann, and Regina Barrera. Faraday’s law, lenz’s law, and conservation of energy. American Journal of Physics, 72(3):376–380, 2004.

[59] Robert Kingman, S Clark Rowland, and Sabin Popescu. An experimental observation of faraday’ s law of induction. American Journal of Physics, 70(6):595–598, 2002.

[60] Jared Paul Phillips, Saeed Yazdani, Wyatt Highland, and Ruihua Cheng. A high sensitivity custom-built vibrating sample magnetometer. Magnetochemistry, 8(8):84, 2022.

[61] Simon Foner. The vibrating sample magnetometer: Experiences of a volunteer. Journal of applied physics, 79(8):4740–4745, 1996.

[62] Wesley Burgei, Michael J Pechan, and Herbert Jaeger. A simple vibrating sample magnetometer for use in a materials physics course. American Journal of Physics, 71(8):825–828, 2003.

[63] JA Gerber, WL Burmester, and David J Sellmyer. Simple vibrating sample magnetometer. Review of Scientific Instruments, 53(5):691–693, 1982.

[64] V Lopez-Dominguez, Adrián Quesada, JC Guzmán-Mínguez, L Moreno, M Lere, J Spottorno, F Giacomone, JF Fernández, Antonio Hernando, and MA García. A simple vibrating sample magnetometer for macroscopic samples. Review of Scientific Instruments, 89(3):034707, 2018.

[65] Chi-Feng Pai, Maxwell Mann, Aik Jun Tan, and Geoffrey SD Beach. Determination of spin torque efficiencies in heterostructures with perpendicular magnetic anisotropy. Physical Review B, 93(14):144409, 2016.

[66] Kohei Ueda, Maxwell Mann, Chi-Feng Pai, Aik-Jun Tan, and Geoffrey SD Beach. Spin-orbit torques in ta/tbxco100-x ferrimagnetic alloy films with bulk perpendicular magnetic anisotropy. Applied Physics Letters, 109(23):232403, 2016.

[67] Wei-Bang Liao, Tian-Yue Chen, Yari Ferrante, Stuart SP Parkin, and Chi-Feng Pai. Current-induced magnetization switching by the high spin hall conductivity α-w. physica status solidi (RRL)–Rapid Research Letters, 13(11):1900408, 2019.

[68] TC Chuang, CF Pai, and SY Huang. Cr-induced perpendicular magnetic anisotropy and field-free spin-orbit-torque switching. Physical Review Applied, 11(6):061005, 2019.

[69] Hao Wu, Seyed Armin Razavi, Qiming Shao, Xiang Li, Kin L Wong, Yuxiang Liu, Gen Yin, and Kang L Wang. Spin-orbit torque from a ferromagnetic metal. Physical Review B, 99(18):184403, 2019.

[70] Nirvana B Caballero, Ezequiel E Ferrero, Alejandro B Kolton, Javier Curiale, Vincent Jeudy, and Sebastian Bustingorry. Magnetic domain wall creep and depinning: A scalar field model approach. Physical Review E, 97(6):062122, 2018.

[71] OJ Lee, LQ Liu, CF Pai, Y Li, HW Tseng, PG Gowtham, JP Park, DC Ralph, and RA Buhrman. Central role of domain wall depinning for perpendicular magnetization switching driven by spin torque from the spin hall effect. Physical Review B, 89(2):024418, 2014.

[72] Xu Zhang, Jian Mao, Meixia Chang, Ze Yan, Yalu Zuo, and Li Xi. Current-induced magnetization switching in pt/co/w and pt/co/w0. 82pt0. 18 structures with perpendicular magnetic anisotropy. Journal of Physics D: Applied Physics, 53(22):225003, 2020.

[73] Qiang Hao and Gang Xiao. Giant spin hall effect and switching induced by spin-transfer torque in a w/co 40 fe 40 b 20/mgo structure with perpendicular magnetic anisotropy. Physical Review Applied, 3(3):034009, 2015.

[74] D Bedau, H Liu, JZ Sun, JA Katine, EE Fullerton, S Mangin, and AD Kent. Spin-transfer pulse switching: From the dynamic to the thermally activated regime. Applied Physics Letters, 97(26):262502, 2010.

[75] RH Koch, JA Katine, and JZ Sun. Time-resolved reversal of spin-transfer switching in a nanomagnet. Physical review letters, 92(8):088302, 2004.

[76] Tian-Yue Chen Tsung-Yu Tsai Cheng-Wei Peng Tsung-Yi Chen, Wei-Bang Liao and Chi-Feng Pai. Current-induced spin − orbit torque efficiencies in w/pt/co/pt heterostructures. Applied Physics Letters, 116(7):072405, 2020.

[77] Shunsuke Fukami, T Anekawa, C Zhang, and H Ohno. A spin–orbit torque switching scheme with collinear magnetic easy axis and current configuration. nature nanotechnology, 11(7):621–625, 2016.

[78] Jiazhi Quan, Xiaotian Zhao, Wei Liu, Long Liu, Yuhang Song, Yang Li, Jun Ma, Shuqiao Li, Xinguo Zhao, and Zhidong Zhang. Enhancement of spin–orbit torque and modulation of dzyaloshinskii–moriya interaction in pt100-xcrx/co/alox trilayer. Applied Physics Letters, 117(22):222405, 2020.

[79] PC Van Son, H Van Kempen, and P Wyder. Boundary resistance of the ferromagnetic-nonferromagnetic metal interface. Physical Review Letters, 58(21):2271, 1987.

[80] Lijun Zhu. Switching of perpendicular magnetization by spin-orbit torque. Advanced Materials, page 2300853, 2023.

[81] Ting-Chien Wang, Tian-Yue Chen, Chun-Te Wu, Hung-Wei Yen, and Chi-Feng Pai. Comparative study on spin-orbit torque efficiencies from w/ferromagnetic and w/ferrimagnetic heterostructures. Physical Review Materials, 2(1):014403, 2018.

[82] Kyeong-Dong Lee Younghun Jo Soonha Cho, Seung-heon Chris Baek and Byong-Guk Park. Large spin hall magnetoresistance and its correlation to the spin-orbit torque in w/cofeb/mgo structures. Scientific reports, 5(1):1–9, 2015.

[83] Yari Ferrante Stuart S. P. Parkin Wei-Bang Liao, Tian-Yue Chen and Chi-Feng Pai. Current-induced magnetization switching by the high spin hall conductivity α-w. Rapid Research Letters, 13(11):1900408, 2019.

[84] A. Ohkawara S. DuttaGupta H. Sato F. Matsukura C. Zhang, S. Fukami; K. Watanabe and H. Ohno. Critical role of w deposition condition on spin-orbit torque induced magnetization switching in nanoscale w/cofeb/mgo. Applied Physics Letters, 109(19):192405, 2016.

[85] Sadamichi Maekawa, Takashi Kikkawa, Hiroyuki Chudo, Jun’ ichi Ieda, and Eiji Saitoh. Spin and spin current—from fundamentals to recent progress. Journal of Applied Physics, 133(2):020902, 2023.

[86] Luqiao Liu, OJ Lee, TJ Gudmundsen, DC Ralph, and RA Buhrman. Current-induced switching of perpendicularly magnetized magnetic layers using spin torque from the spin hall effect. Physical review letters, 109(9):096602, 2012.

[87] ZR Tadisina, A Natarajarathinam, and S Gupta. Magnetic tunnel junctions with co-based perpendicular magnetic anisotropy multilayers. Journal of Vacuum Science & Technology A: Vacuum, Surfaces, and Films, 28(4):973–978, 2010.

[88] Gouri Sankar Kar, Woojin Kim, Taiebeh Tahmasebi, Johan Swerts, Sofie Mertens, Nancy Heylen, and Tai Min. Co/ni based p-mtj stack for sub-20nm high density stand alone and high performance embedded memory application. In 2014 IEEE International Electron Devices Meeting, pages 19–1. IEEE, 2014.

[89] S Ishikawa, H Sato, M Yamanouchi, S Ikeda, S Fukami, F Matsukura, and H Ohno. Magnetic properties of mgo-[co/pt] multilayers with a cofeb insertion layer. Journal of Applied Physics, 113(17):17C721, 2013.

[90] Kay Yakushiji, Hitoshi Kubota, Akio Fukushima, and Shinji Yuasa. Perpendicular magnetic tunnel junctions with strong antiferromagnetic interlayer exchange coupling at first oscillation peak. Applied Physics Express, 8(8):083003, 2015.

[91] C-J Lin, GL Gorman, CH Lee, RFC Farrow, EE Marinero, HV Do, H Notarys, and CJ Chien. Magnetic and structural properties of co/pt multilayers. Journal of Magnetism and Magnetic Materials, 93:194–206, 1991.

[92] Jacob Torrejon, Junyeon Kim, Jaivardhan Sinha, Seiji Mitani, Masamitsu Hayashi, Michihiko Yamanouchi, and Hideo Ohno. Interface control of the magnetic chirality in cofeb/ mgo heterostructures with heavy-metal underlayers. Nature communications, 5(1):4655, 2014.

[93] Lijun Zhu and Daniel C Ralph. Strong variation of spin-orbit torques with relative spin relaxation rates in ferrimagnets. Nature Communications, 14(1):1778, 2023.